공학석사 학위논문

Thermomechanical borehole stability analysis by true triaxial experiment and discrete element modeling

진삼축 실험과 개별요소법을 이용한 열-역학적 공벽안정성 해석

2019 년 8 월

서울대학교 대학원

에너지시스템공학부

윤 동 영

Thermomechanical borehole stability analysis by true triaxial experiment and discrete element modeling

지도 교수 민 기 복

이 논문을 공학석사 학위논문으로 제출함
2019 년 7 월

서울대학교 대학원
에너지시스템공학부
윤 동 영

윤동영의 공학석사 학위논문을 인준함
2019 년 7 월

위 원 장 전 석 원 (인)

부위원장 민 기 복 (인)

위 원 송 재 준 (인)

Abstract

Thermomechanical borehole stability analysis by true triaxial experiment and discrete element modeling

Dongyoung Yoon
The Graduate School
Department of Energy Systems Engineering
Rock Mechanics & Rock Engineering Laboratory
Seoul National University

Ensuring borehole stability is a significant issue that should be considered for deep underground engineering where large magnitude of in situ stress has high possibility to cause borehole breakout. Borehole breakout occurs by stress concentration on near borehole wall by redistribution of stress when borehole is drilled and appear as symmetrical V-shaped notch in the direction to minimum horizontal stress. Moreover, when it comes to engineering systems where temperature changes significantly within the borehole, such as geothermal development or nuclear waste disposal, temperature effect should also considered for borehole stability.

This thesis is mainly divided in two parts which are laboratory

test and numerical test. Laboratory test was conducted on 100 mm cubic size cement mortar specimen with 20 mm borehole. True-triaxial test machine was used and failure was monitored by acoustic emission and camera inserted inside borehole. Also, X-ray CT scanning technique was utilized to observe borehole shape after breakout. Significant strengthening effect of vertical stress on borehole breakout was observed. Also, the result was analyzed by Mogi-coulomb and Mohr-coulomb failure criteria and showed Mogi-coulomb criteria reflected the effect of vertical stress on borehole breakout. In addition to mechanical test, heater test was also conducted. Temperature was increase to 130 ℃ from outer surface of specimen with true-triaxial confining stress simultaneously. Extra borehole breakout by thermal effect was observed.

Numerical simulation was performed by discrete element method and laboratory result was reproduced. Flat-joint contact model was assigned to represent rock-like brittle material. Mechanical modeling results matched well with laboratory test results both on failure procedure and breakout patterns. Also, Thermal code was implemented to reproduce heater test numerically. Alike laboratory test, extra failure by temperature rise was occurred on specimen surface and on near borehole wall. This numerical modeling will provide the possibility of site-specific study to investigate underground conditions favorable to severe borehole instability.

This laboratory and numerical test reproducing field situation, by considering the effect of in situ stress and temperature change simultaneously, are expected to pave the way for various underground engineering such as geothermal development or nuclear

waste disposal system.

Keyword : Borehole breakout, Nuclear waste disposal, Geothermal energy, thermo-mechanical modeling, true-triaixal laboratory test, Discrete element modeling.

Student Number : 2017-25342

Contents

Lists of tables

Lists of Figures

Chapter 1. **Introduction**

1.1 Borehole breakout

One of the prerequisites for the most of engineering projects in underground conditions is drilling a borehole (or tunnel) subjected to in situ stresses. When borehole is drilled, the original state of stress in the rock mass will change and stress concentrates near the borehole. If this stress exceeds rock strength, the failure, so called borehole breakout or spalling, occurs. As shown in Figure 1.1, borehole breakout is a commonly observed phenomenon which enlarge the borehole in the direction of minimum horizontal stress (Zoback et al. 1985). Usually, borehole breakout can provide an information of in situ stress direction or magnitude so with aid of logging technique borehole breakout is utilized as in situ stress indicator (Bell and Gough 1979; Barton, Zoback, and Burns 1988; Shamir and Zoback 1992; Townend and Zoback 2004; Chang et al. 2010). Moreover, as the target depth gets deeper, because of the limitations of other methods, borehole breakout as in situ stress indicator gets more important.

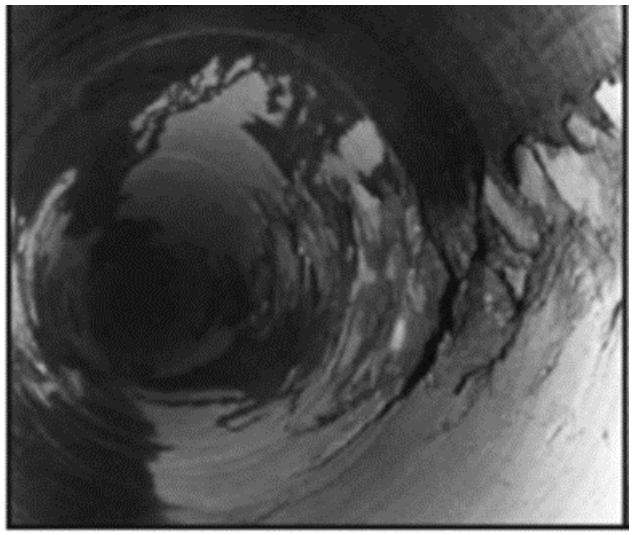

Figure 1.1: Breakout observed by downhole camera. (Tingay et al. 2008).

However, severe breakout causes several problems. For instance, if rock fragments induced by breakout make pipe stuck as Figure 1.2, or close the borehole, it will delay the project or require extra operations such as side-tracking, fishing and reaming which would cause financial losses or even make drilling to be renounced. Moreover, when the borehole is used for nuclear waste fuel storage, breakout will change the hydraulic conductivity near wall and influence the safety of the system (Souley et al. 2001; Yuan and Harrison 2006). As a result, managing the borehole breakout is one of the imperative issues on many underground engineering projects.

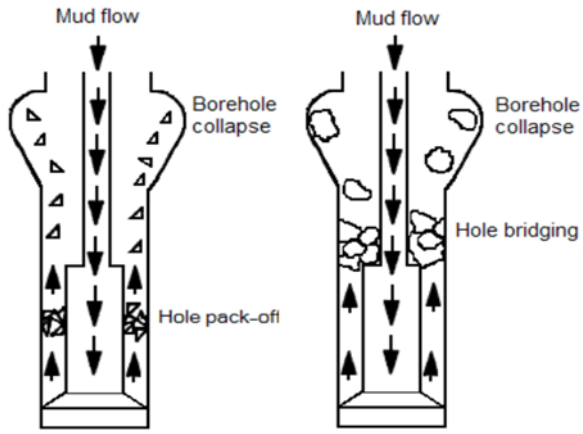

Figure 1.2: Stuck pipe problem due to severe borehole collapse (Al-Ajmi 2006)

On the other hand, rock mass response to thermal-loading is also one of indispensable factor to take into account where borehole temperature conditions vary significantly from ambient conditions. Thermal loading usually occurs by two reasons, 1) mismatch between thermal expansion coefficients of adjacent mineral grains, 2) thermal stresses induced by temperature gradient (Jansen et al. 1993a). In this case, thermal-loading is another important factor that affects borehole stability additional to in situ stress. For example, underground storage of radioactive nuclear waste will produce high temperature by fission of waste and will diffuse to the surrounding rocks and cause thermal gradient near the wall which subsequently induce thermal-loading. In addition, the thermal-loading is expected to occur where the boreholes for geothermal development are drilled at deep level. Usually geothermal development requires the depth

more than 4Km. Because of typical thermal gradient in underground, the temperature of rock mass at this level is more than 100 ℃. This high geothermal temperature will heat and recover temperature of cooled borehole by injected fluid such as drilling mud or fluid for engineering operations such as hydraulic fracturing. This situation will also make thermal-loading takes place. Subsequently, Induced thermal-loading will change the stress state near the wall to more critical to breakout

1.2 Literature review

1.2.1 Experimental test

V-shaped notch are the most commonly observed breakout patterns which is developed by either shear failure or tensile failure or the combination of two. Figure 1.3 shows that this V-shape failure was possible to reproduce by laboratory test. Previous studies pointed out that the failure patterns are dependent on the grain-scale micro characteristics of rock type, showing shear failure type breakout on limestone and continuous spalling off by tensile failure from granite (Haimson and Song 1993; Lee and Haimson 1993). However, due to the difficulty of specimen preparation and complexity of testing procedures, most of the experiments were conducted on biaxial condition although it is true-triaxial state in real engineering field. Moreover, even if they were conducted on a true-triaxial conditions, the experiments did not focused on the effect of intermediate principal stress on borehole stability. However, intermediate principal stress effect on underground excavation in the field was emphasized by several researchers (Single et al. 1998; Ewy 1999). As such importance of quantifying the true-triaxial effect on borehole breakout burgeoned. Some researchers have investigated the true-triaxial effect on rock failure, showing there is a significant

strengthening effect of intermediate principal stress on rock failure and suggested a new criterion for rock failure (Haimson and Chang 2000; Haimson ; Mogi 1971).

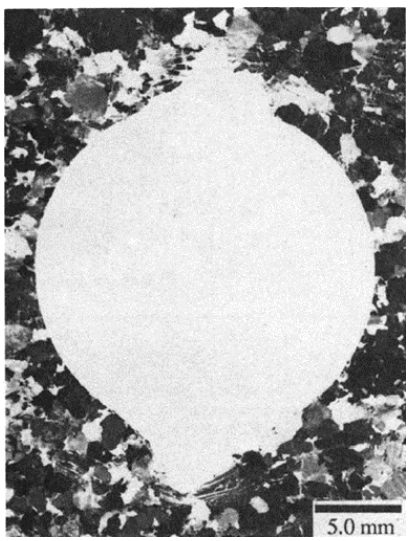

Figure 1.3: V-shaped notch observed by laboratory test. Cross section view of granite specimen. (Lee and Haimson 1993).

Thermally induced failure was investigated in laboratory by heater test using hollow cylinder specimen resulting tensile failure from the outer surface which then propagated inward (Ishida 2004; Jansen et al. 1993b). This thermal fracture was produced mainly by the temperature gradient throughout the specimen that generates compression stress near borehole and tensile stress near the outer surface (Figure 1.4). However, this experimental tests show limitation since they did not consider the existing in situ stress. Numerical study have shown that the failure pattern will be different with existence of confining stress in boundary (Zhao 2016).

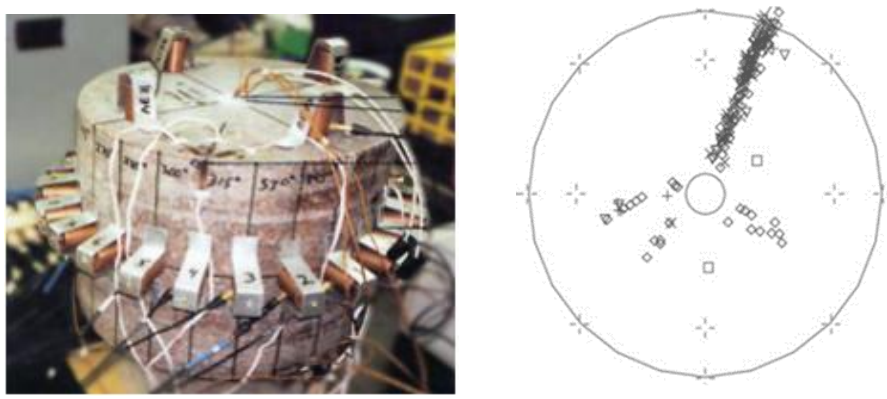

Figure 1.4: LdB granite specimen set up for heater test and post-failure AE events. Heater is inserted inside the borehole and AE transducers bounds the specimen (Wanne and Young 2008).

Aside from laboratory experiment, efforts to conduct a field study on mechanical and thermo-mechanical failure have been made. Alike laboratory test result, failure was increased after borehole excavation and temperature rise as illustrated in Figure 1.5. However, these field study which revealed the significant thermal effect on failure is mainly due to the increased tangential stresses near the borehole wall as depicted in Figure 1.6 (Andersson, Martin, and Stille 2009; Read 2004). It means that compressive failure near wall is more important than tensile failure regarding thermal induced borehole stability issue.

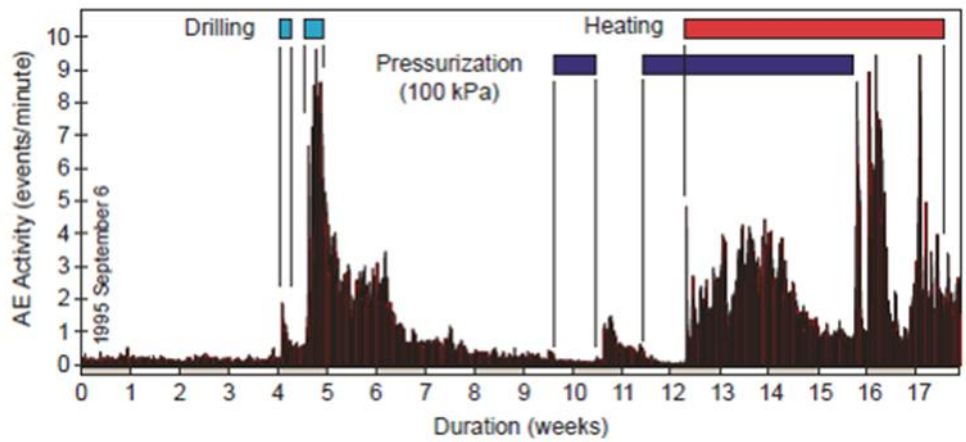

Figure 1.5: AE activity during field test procedure including drilling, pressurization and heating. Increased AE activity after drilling and heating can be observed (Read 2004).

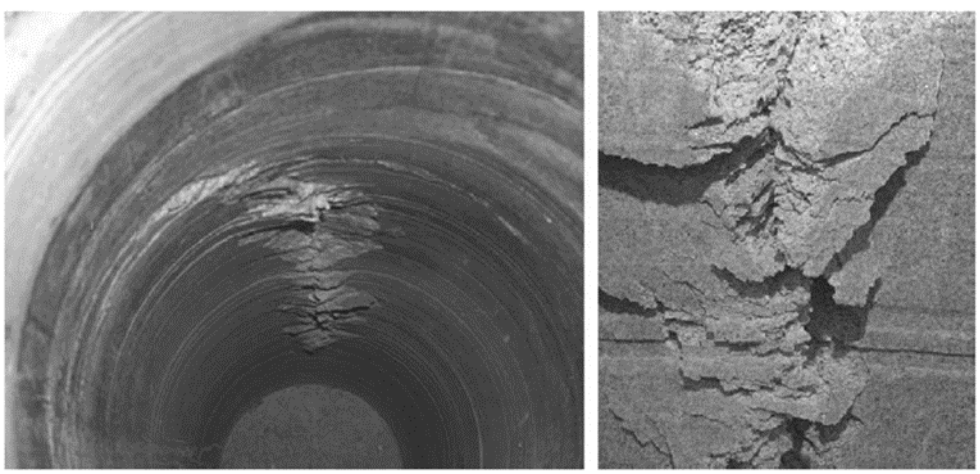

Figure 1.6: Additional compression failure around borehole wall due to temperature rise (Read 2004).

1.2.2 Numerical test

Parallel with laboratory experiments, numerical works strived to investigate the mechanism of borehole breakout. Among many different numerical approach, because of its advantages in modeling failure phenomena, particle based discrete element method (DEM) modeling has been used widely for simulating borehole breakout (Potyondy and Cundall 2004).

DEM modeling simulated the V-shaped mechanical breakout patterns from laboratory test well (Fakhimi et al. 2002; Lee, Moon, and Haimson 2016; Potyondy 2017). Moreover, Pattern of breakout failure of anisotropic rock was also simulated by DEM and validated by laboratory test result (Duan, Kwok, and Pierce 2016; Park and Min 2015; Park et al. 2018). The simulation of thermally induced failure of cylindrical specimen was also successful using DEM with heat-flow code (Wanne and Young 2008). DEM was also capable to model the reduced compressive and tensile strengths of intact rock by thermal loading (Zhao 2016). Moreover, simulation was also conducted to model the field study results (Koyama et al. 2013; Wanne 2009). The simulation results were correspondent to field test observations. However, the scale was too large for computation time so all the DEM simulation for field test was conducted on two dimension.

1.3 Objectives and Motivations

Field scale study could be the best option but definitely not cost-effective, and would be even more difficult in deep underground situations like depth about 3~5Km or more. As a result, laboratory test could be the alternative way to study the condition underground, and the result will give more realistic insight as the conditions of the test be more analogous to real field conditions. For these reasons, in this study, laboratory experiment subjected to true-triaxial load assigning high temperature simultaneously is conducted.

In detail there are two main objectives for this true-triaxial laboratory test. First is to capture the effect of vertical stress on borehole stability and utilize a proper failure criterion needed to relate borehole breakout in true-triaxial state. Second is to quantify and qualify the effect of thermally induced failure. Obviously, this study will deepen the understanding on failure near the borehole in deep underground while engineering projects progress.

Moreover, the mechanical and thermo-mechanical numerical study using DEM is also conducted and validated with laboratory test result. This will give a further understanding on the mechanism of borehole breakout. It is expected to improve possibilities of site specific modeling for optimizing engineering design especially for deep borehole disposal or geothermal development.

Chapter 2. **Background and theory**

2.1 Failure criteria

To analyze rock failure, numerous failure criteria have been suggested, e.g., Mohr−coulomb, Hoek−Brown, Mogi, Mogi−coulomb (Al−Ajmi and Zimmerman 2006; Jaeger 2007). In this study, to analyze laboratory test result, two typical failure criteria which is Mohr−coulomb and Mogi−coulomb has been utilized.

Mohr−coulomb criterion is the simplest and widely used one. This criterion premises that failure in rock takes place as sliding of plane due to shear stress τ acting along that plane. However, this sliding is resisted by cohesion c and internal friction ϕ of rock. So the shear stress has to overcome this resistance to occur rock failure. This consideration of Mohr−Coulomb criterion can be expressed in terms of maximum and minimum principal stress σ_1 and σ_3, so failure occurs when satisfies following equation:.

$$\sigma_1 = C_0 + q\sigma_3 \qquad (2.1)$$

where Uniaxial compressive strength C_0 and q are parameters that related to cohesion and internal friction angle as

$$\mathrm{q} = tan^2(\pi/4 + \emptyset/2), \quad C_0 = 2c \cdot \cos(\emptyset)/(1 - \sin\emptyset) \qquad (2.2)$$

However, Mohr−coulomb criterion assumes that failure ignores the effect of intermediate principal stress

(Mogi 1971) first designed true triaxial test apparatus to study the effect of intermediate principal stress σ_2 on rock failure. This apparatus was able to conduct test where stress condition differs from conventional triaxial test condition. The test was conducted on Dolomite and Limestone. Result showed that the intermediate principal stress has strengthening effect. Further he showed this true−triaxial test results fit in a single failuire criterion when plotted in octahedral stress strass τ_{oct}− mean normal stress $\sigma_{m,2}$ domain where octahedral shear stress and mean normal stress, defined by

$$\tau_{oct} = \frac{1}{3}\sqrt{(\sigma_1 - \sigma_3)^2 + (\sigma_2 - \sigma_3)^2 + (\sigma_3 - \sigma_1)^2} \tag{2.3}$$

$$\sigma_{m,2} = (\sigma_1 + \sigma_3)/2$$

and suggested a new failure criterion as function below:

$$\tau_{oct} = f(\sigma_{m,2}) \tag{2.4}$$

Where f is nonlinearly increasing function. Mogi criterion explains the rock failure well. However, since the function f is nonlinear, true−triaxial test should be conducted to acquire the parameters related to this function which makes this criterion not practical.

(Al−Ajmi and Zimmerman 2006) suggested to replace function f as a linear function defined by

$$\tau_{oct} = a + b\sigma_{m,2} \tag{2.5}$$

where parameter **a** and **b** can be easily obtained by traditional triaxial test since theses parameters are related to cohesion and internal friction angle, as follows:

$$\mathrm{a} = \frac{2\sqrt{2}}{3} c \cdot cos\emptyset, \qquad b = \frac{2\sqrt{2}}{3} sin\emptyset \tag{2.6}$$

They named this modified failure criterion as Mogi−coulomb failure criterion. The data of combined previous conventional triaxial test results, were plotted in Mogi domain ($\tau_{oct} - \sigma_{m,2}$) and showed that Mogi−coulomb criteria well fits the results as depicted in Figure 2.1.

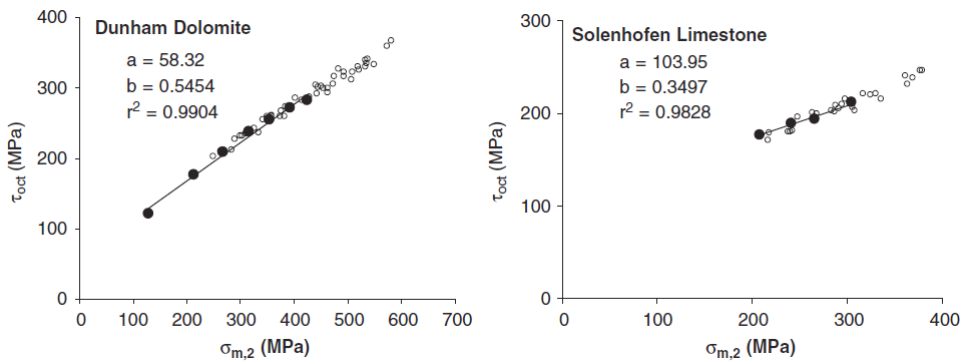

Figure 2.1: Mogi-coulomb failure criterion, fitted to true-triaxial test results (solid) and conventional triaxial test results (open). left: Dunham dolomite, right: Solenhofen Limestone (Al-Ajmi and Zimmerman 2006).

2.2 Discrete Element Method

2.2.1 Flat Joint Contact Model

As explained by pioneering work by (Potyondy 2012), the flat joint contact model (FJM) simulates dense packing of non-uniform rigid circular or spherical particles with notional surface interface between the particles. Then the mechanical behavior of this dense packing particles are simulated by the distinct element method using Particle Flow Code (PFC) 2D and 3D (Itasca 2014; Itasca 2015). Flat joint contact model was developed to overcome the low ratio of UCS/BTS of parallel bonded particle model considering the high ratio of this value for real intact brittle rock.

During numerical UCS test for parallel bonded-particle model peak load is controlled by tensile strength of contact material which is determined to match BTS so there is a limitation in increasing UCS. However, as illustrated in Figure 2.2, in flat joint contact model, by resisting moments during the UCS test after contact breakage, tensile strength of contact model less affects the UCS of numerical specimen and instead, shear strength of contact model determines the UCS. For this reason flat joint contact model makes it possible to match high ratio of UCS/BTS for intact brittle rock.

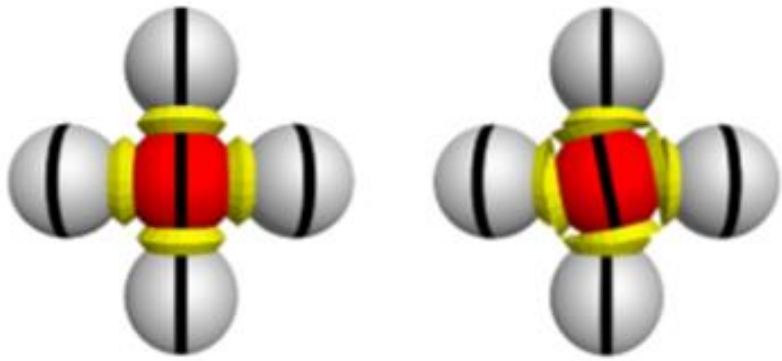

Figure 2.2: Flat joint contact model with four unbonded and frictionless contacts. Each figure shows situation before (left) and after (right) the imposed rotation. Surrounding interface resists the rotation of central particle (Potyondy 2018).

Extensive modeling through PFC has been conducted and by assigning proper microparameters, the flat joint model has matched rock properties of Aspo diorite, Lac du bonnet granite and Castlegate sandstone well (Potyondy 2012; Potyondy 2017; Potyondy 2018).

Numerical model alternates law of motion and force–displacement law for each time steps. Schematic model of relative motion of the notional surfaces at the contact is shown in Figure 2.3. This relative motion can be defined by relative translational velocities and rotational velocities:

$$\dot{U} = \dot{x_c}^{(2)} - \dot{x_c}^{(1)}$$
$$\dot{\theta} = \omega^{(2)} - \omega^{(1)} \quad (2.7)$$

where $\dot{x_c}^{(i)}$ is translational velocity, $\omega^{(i)}$ is rotational velocity for particle (i) at the contact location and particle centroid, respectively.

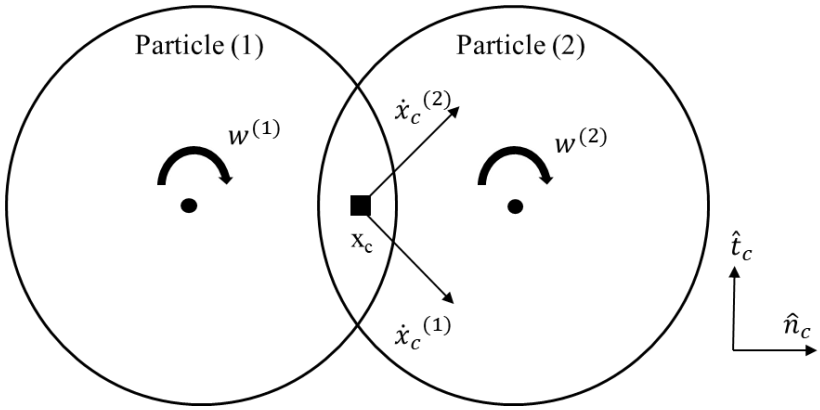

Figure 2.3: Conceptual model of motion at the notional surface.

Equation (2.7) can be rewritten as:

$$\begin{aligned}\dot{U} &= \{(\dot{x}_c^{(2)} - \dot{x}_c^{(1)}) \cdot \hat{\boldsymbol{n}}_{\boldsymbol{c}}\}\,\hat{\boldsymbol{n}}_{\boldsymbol{c}} + \{(\dot{x}_c^{(2)} - \dot{x}_c^{(1)}) \cdot \hat{\boldsymbol{t}}_{\boldsymbol{c}}\}\,\hat{\boldsymbol{t}}_{\boldsymbol{c}} \\ &= \dot{U}_n \hat{\boldsymbol{n}}_{\boldsymbol{c}} + \dot{U}_s \hat{\boldsymbol{t}}_{\boldsymbol{c}}\end{aligned} \tag{2.8}$$

$$\dot{\theta} = \omega^{(2)} - \omega^{(1)} = \dot{\theta}\hat{\boldsymbol{k}}$$

where $\dot{U}_n$ and $\dot{U}_s$ are the relative translational velocities to normal and tangential direction at the middle surface respectively, and $\dot{\theta}$ is the relative rotational velocity. Following the law of motion, the displacement and rotational increments at each time step Δt can be derived from obtained relative velocities as:

$$\begin{aligned}\Delta\mathbf{U} &= \left(\dot{U}_n \Delta \mathrm{t}\right)\hat{\boldsymbol{n}}_{\boldsymbol{c}} + \left(\dot{U}_s \Delta \mathrm{t}\right)\hat{\boldsymbol{t}}_{\boldsymbol{c}} = \Delta\dot{U}_n \hat{\boldsymbol{n}}_{\boldsymbol{c}} + \Delta\dot{U}_s \hat{\boldsymbol{t}}_{\boldsymbol{c}} \\ \Delta\boldsymbol{\theta} &= \left(\dot{\theta}\Delta \mathrm{t}\right)\hat{\boldsymbol{k}} = \Delta\theta\hat{\boldsymbol{k}}\end{aligned} \tag{2.9}$$

Then, total relative motion is calculated by:

$$\begin{aligned} U_n &= U_n + \Delta U_n, \\ U_s &= U_s + \Delta U_s, \\ \theta &= \theta + \Delta\theta \end{aligned} \tag{2.10}$$

As mentioned previously, force displacement law is followed after obtaining the relative motion, to update contact force ($\boldsymbol{F_c}$) and moment ($\boldsymbol{M_c}$).As illustrated in Figure 2.4 the interface is discretized into elements and each elements bears a fore ($\boldsymbol{F}^{(e)}$) and moment ($\boldsymbol{M}^{(e)}$).

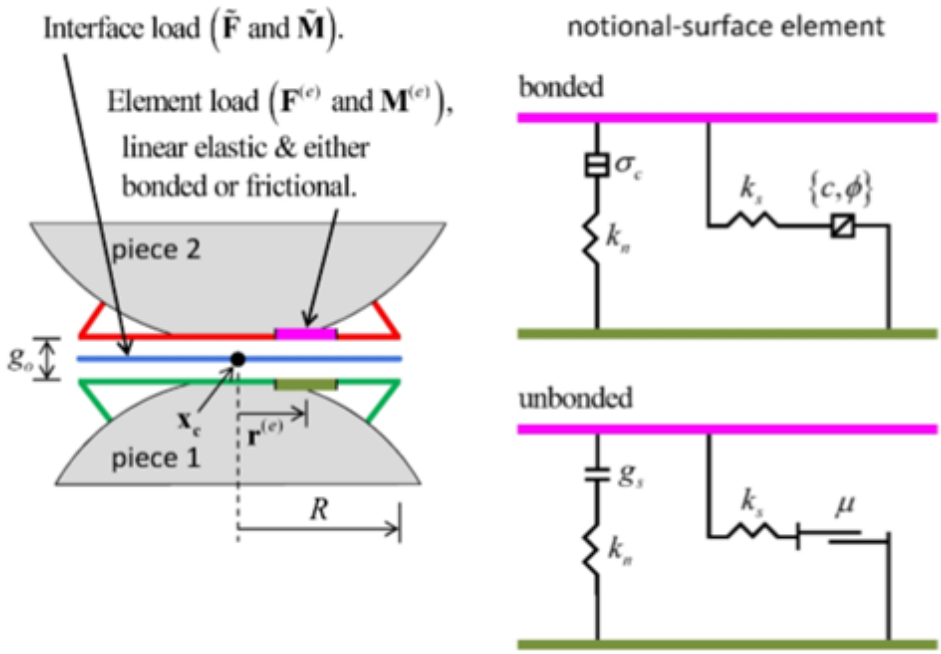

Figure 2.4: Schematic view of flat joint contact interface and its element (Potyondy 2018).

The relationship between contact force and moment and element force and moment can be expressed as:

$$F_c = \tilde{F} = \sum_{\forall e} F^{(e)}$$
$$M_c = \tilde{M} = \sum_{\forall e} \left\{ \left(r^{(e)} \times F^{(e)} \right) + M^{(e)} \right\} \quad (2.11)$$

By utilizing force displacement law to each element, the element contact force and moment is updated. Each element is either bonded or unbonded, and breakage of element contributes to partial damage of the interface. The behavior of bonded and unbonded elements are illustrated in Figure 2.5, and Figure 2.6 respectively. Bonded element behave as linear elastic until strength limit reaches and when it exceeds this limit, element became unbonded. On the other hand, unbonded element has no resistance on tensile stress and behave elastically linear to compression stress and slip occurs by shear force with coulomb limit.

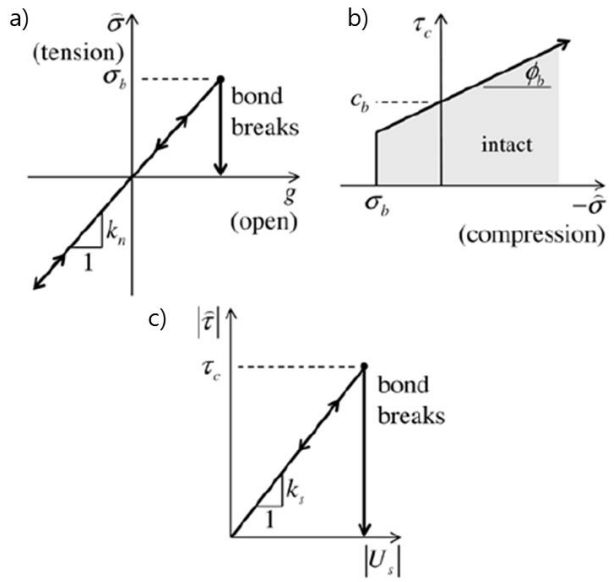

Figure 2.5: Behavior of bonded element (a) normal stress to element gap, (b) shear stress to relative shear displacement and (c) failure envelope (Potyondy 2018).

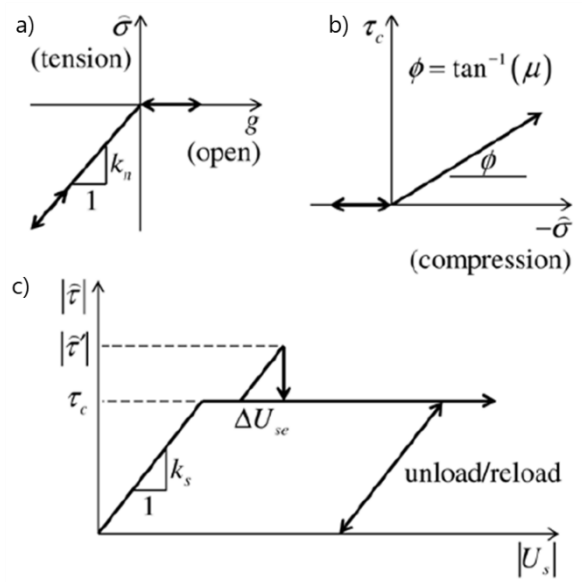

Figure 2.6: Behavior of unbonded element (a) normal stress to element gap, (b) shear stress to relative shear displacement and (c) slip envelope (Potyondy 2018).

2.2.2 Thermal Calculation

Thermal Code in PFC assumes that thermal material is consists of thermal pipes (contacts between particles) and heat reservoirs (particles) and simulates heat conduction by heat flow between these heat reservoirs through thermal pipes following Fourier's law:

$$Q = kA\frac{\Delta T}{L} \tag{2.12}$$

where Q is heat flow, k is thermal conductivity of the heat pipe, A is area of the contact point, ΔT is the temperature difference between the two particles and L is the length of thermal pipe (distance between centers of two particles).

When heat conduction take place, temperature of a particle is updated following the equation below:

$$dT = \frac{Q\Delta t}{Cm} \tag{2.13}$$

where dT is change in temperature, C is specific heat of the particle, m is mass of particle, and Δt is the thermal time step.

Temperature change of the particle will successively induce thermal strain which represented my modifying the radius of particle. The increment of radius dr by temperature change is obtained by:

$$dr = \alpha_T r dT \tag{2.14}$$

where α_T is thermal expansion coefficient of particle. If particles are in contact, this change in radius will affect the surface gap and finally surface stress, which can also said to be thermally induced stress. The upper mentioned procedure of PFC thermal algorithm is illustrated in Figure 2.7

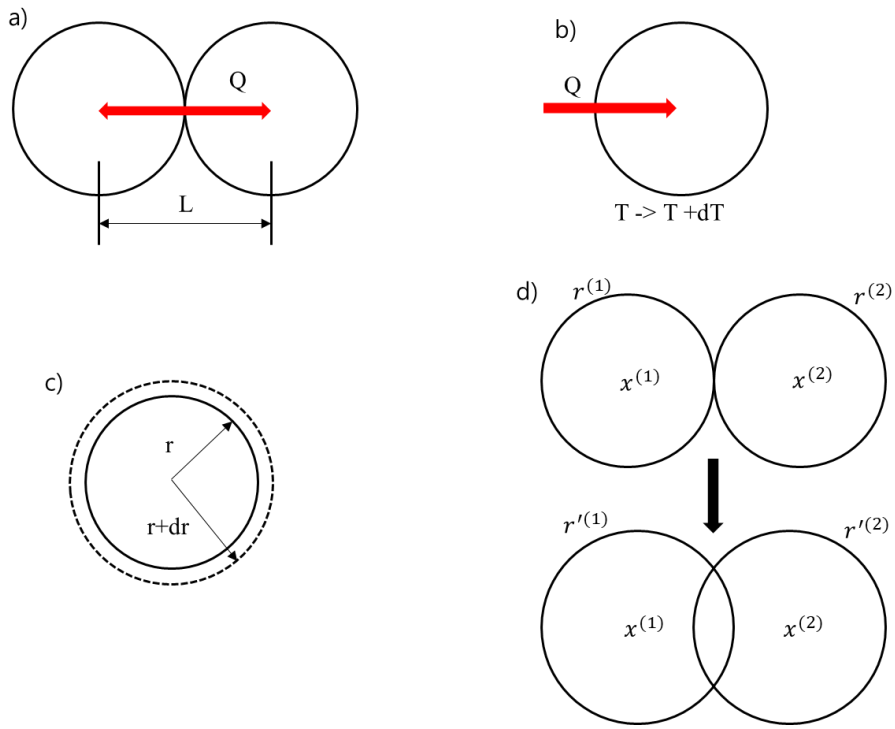

Figure 2.7: PFC thermal algorithm (a) Heat flow, (b) Temperature change, (c) Particle expansion, and (d) Change of surface gap (Koyama et al. 2013).

Chapter 3. **Laboratory test**

3.1 Test description

3.1.1 Specimen and its properties

In this study, for its brittleness, cement mortar which is rock-like material has been used for the laboratory test. Ultra rapid hardening cement (UNION Grout JM type) was used to make cement mortar specimen. Ultra rapid hardening cement has advantages for laboratory test specimen because it requires relatively short time of curing to acquire targeted strength and also after 4 days of curing, the strength varies very little. Cement mortar was molded by aluminum frame with inserted PVC cylinder to make circular opening as depicted in Figure 3.1. To keep material properties constant as possible, every specimen was mixed with same ratio of cement to water weight as 4:1 and was cured for 4 to 6 days. The completed cement mortar specimen for laboratory test is also shown in figure 3.1. The size of specimen is 100mm cubic with 20mm dimeter open hole.

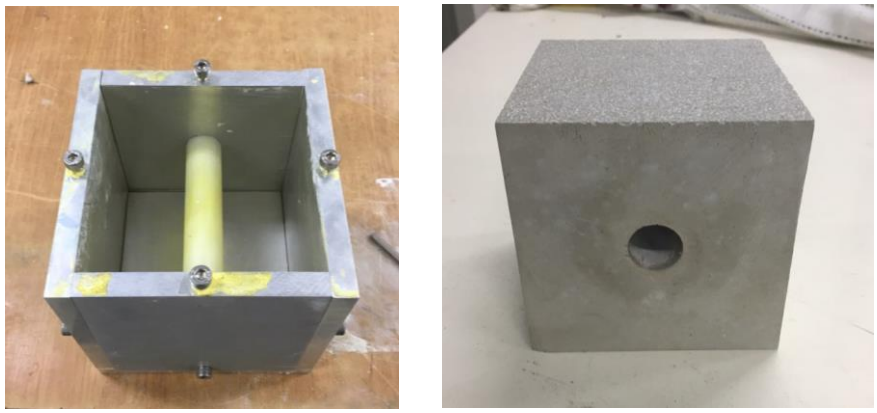

Figure 3.1: Aluminum molding frame and cement Mortar specimen used for laboratory test. 100 mm cubic size with 20 mm diameter borehole specimen is used.

.

In addition to cubic specimen, cylindrical specimens were also cured to conduct standard laboratory test to determine mechanical properties of cement mortar specimen. Five uniaxial compression test and five brazilian tensile tests were conducted and size of the cylindrical specimen were 100 mm height and 25 mm thick respectively, with same diameter of 50 mm. In addition, strain gauge was attached in cylindrical specimen during uniaxial compression test to obtain elastic modulus and poisson's ratio. The mechanical properties of the cement mortar are summarized in Table 3.1. One thing to notice is that triaxial test was not conducted on mortar sample so, the value of internal friction angle was referred from (Nan 2017) and cohesion was calculated from this value.

Table 3.1: Material properties of cement mortar specimen.

Properties	Value
Elastic modulus (E)	25 GPa
Poisson's ratio (**ν**)	0.25
Rock density	1850 kg/m^3
Uniaxial compression strength	38 MPa
Brazilian tensile strength	2.3 MPa
Internal friction angle	31 °
Cohesion	10.5 MPa

3.1.2 Laboratory test system

The experimental system was composed of loading frames, Pressure generator, Temperature penal, AE sensors, camera and control PCs for pressure control and AE monitoring respectively. The overall view and close up view of the true-triaxial experimental system is depicted in Figure 3.2 and Figure 3.3, respectively. The plate size at each load frame is 95 mm X 95 mm square and maximum force capacity is 1100 kN. Heating elements were inserted in each plate and controlled by temperature penal attached in true-triaxial test machine. The maximum capacity of temperature rise for this system is 150 ℃. The conceptual model of loading plate is illustrated in Figure 3.4. All cables were pulled out from the loading plate and connected to relevant control devices.

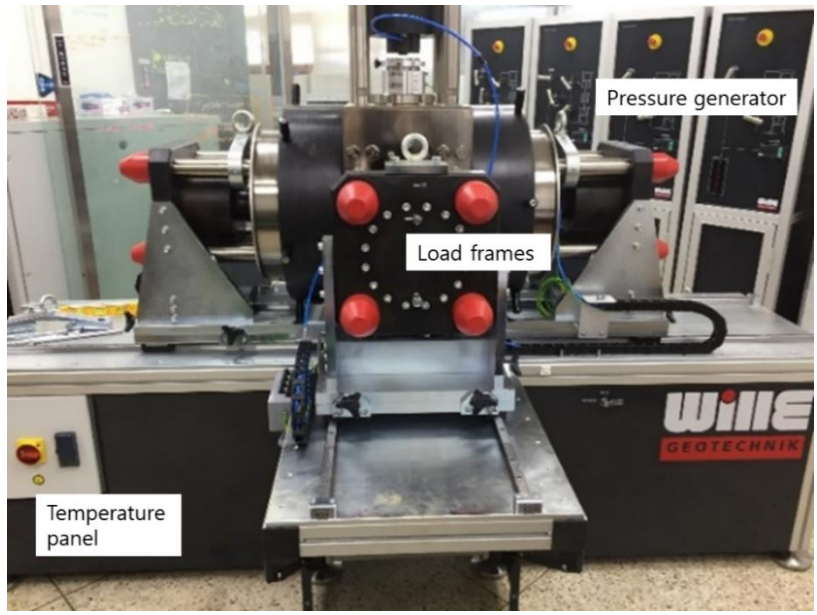

Figure 3.2: Overall view of true-triaxial test loading system

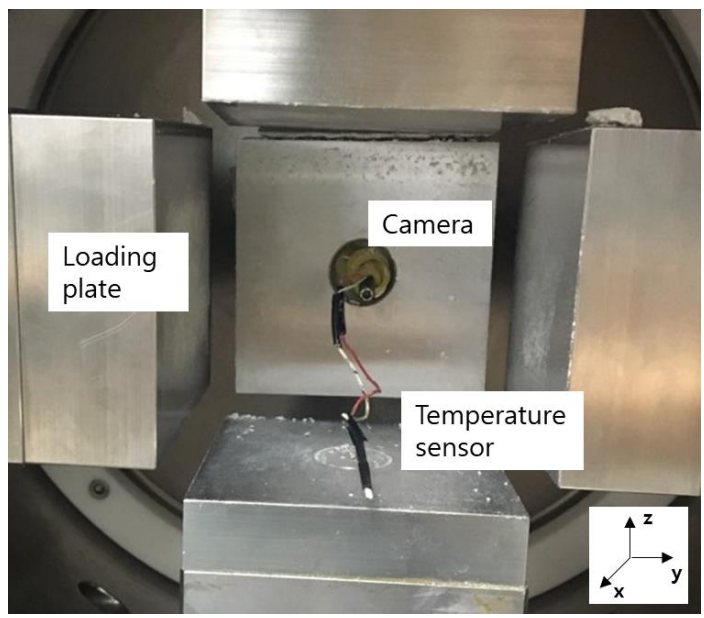

Figure 3.3: Close up view of true-triaxial test system. Axis for identifying each plate directions are also shown.

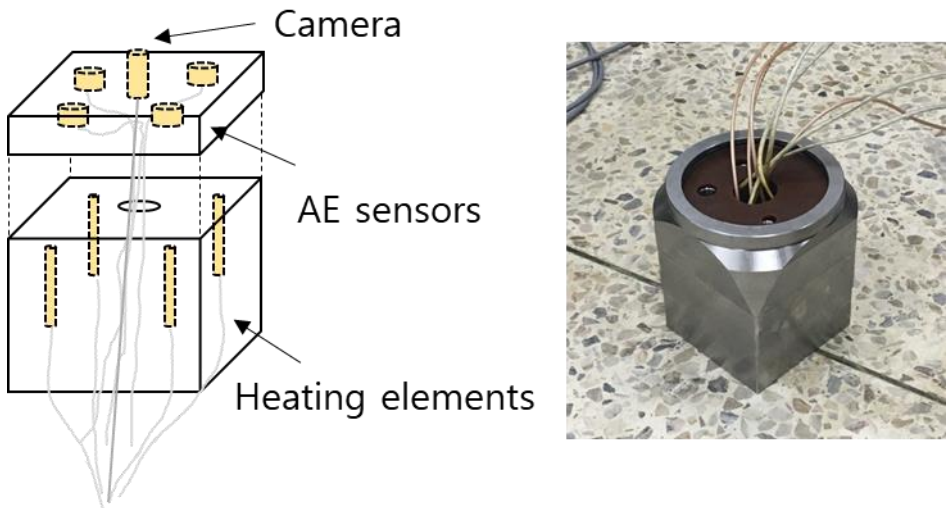

Figure 3.4: Schematic view and picture of loading plate and inserted sensors and elements

Monitoring of failure was done by camera and AE sensors. As can be shown in Figure 3.3, 5 mm diameter size camera was inserted in x-axis plate. Since borehole was aligned with x-axis, camera was placed inside the borehole and provided real-time visual data of borehole wall condition (Figure 3.5). Also, in this study, X axis was set to be vertical stress and Y axis and Z axis be minimum horizontal stress and maximum horizontal stress, respectively.

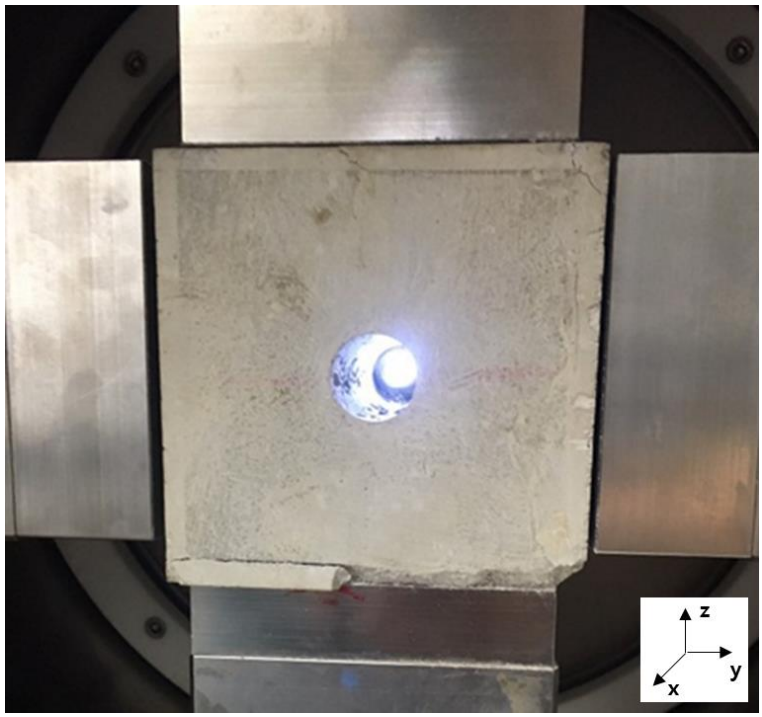

Figure 3.5: Specimen placed in true-triaxial test machine. Camera is positioned inside the borehole. LED light is emitted from the camera.

When sudden release of elastic energy take places by initiation or propagation of microcracks and other irreversible deformation of material, transient stress waves propagates as acoustic emission (AE) (ASTM 2006). Therefore, numerous studies applied AE measurement for analyzing failure of rock or rock-like materials (Liu et al. 2015; Michlmayr, Cohen, and Or 2012). Total eight AE sensors were used for detecting failure. Four sensors were placed inside at each loading plate which were aligned in y axis. Because of the true-triaxial loading condition, it was impossible to attach AE sensors directly to the specimen surface

and 5mm gap was existed between AE sensor and specimen. The placed sensors on loading plate and schematic view of AE sensors location relative to specimen are sown in Figure 3.6, respectively. After placing the sensors, springs were placed behind the sensors to ascertain tight contact with plate. In this study, R15S sensor from MISTRAS was used since it was applicable at the high temperature environment up to 177 ℃.

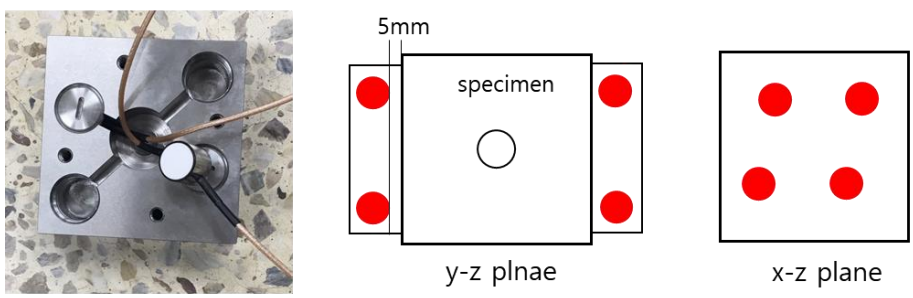

Figure 3.6: AE sensors placed in loading plate and its schematic position relative to test specimen.

In this study, AEwin software from PAC was applied to record and post process the acquired AE data. Absolute energy was utilized for estimating rock failure. (Keshavarz 2009) pointed out that cumulate AE energy is effective parameter of predicting catastrophic failure of material because sharp increase of this parameter occurs in each phase of the failure process. Figure 3.7 illustrates the main parameters and idealized wave form of AE event.

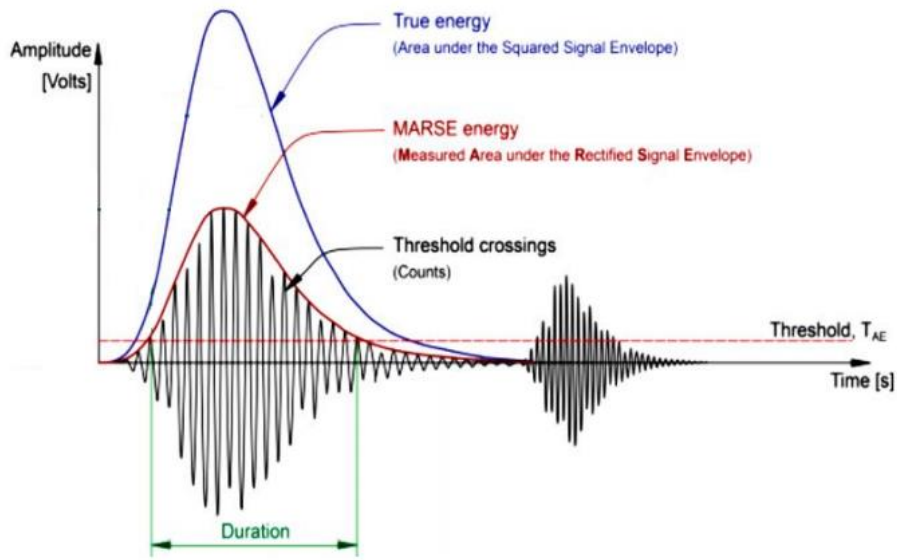

Figure 3.7: Main parameters and waveform of AE event (Gholizadeh 2015).

Absolute energy is parameter refers the true energy of an AE event. This parameter is commonly expressed in atto−joules (1 aJ = 10^{-18} J) and vales are obtained as:

$$Absolute\ \ energy = \frac{1}{R} \sum_{duration} {V_i}^2 \cdot \Delta t \qquad (3.1)$$

where R is sensor impedance (10 KΩ), V_i is sensor voltage at section i and Δt is time step for calculation.

3.1.3 Test set-up and procedure.

Loading mode for loading test is depicted in Figure 3.8. Each three different loading axis was controlled by separate servo-controlled system. At first stage, All true-triaxial loading, which are vertical stress (S_v) minimum horizontal stress (S_h) and maximum horizontal stress (S_H) raised simultaneously to avoid extreme stress state before targeted stress state reached. However, when S_v or S_h reached targeted value, they were held constant while S_H was increased till borehole breakout initiated and developed. All true-triaxial stresses were increased linearly at a constant rate of 0.01 MPa/s.

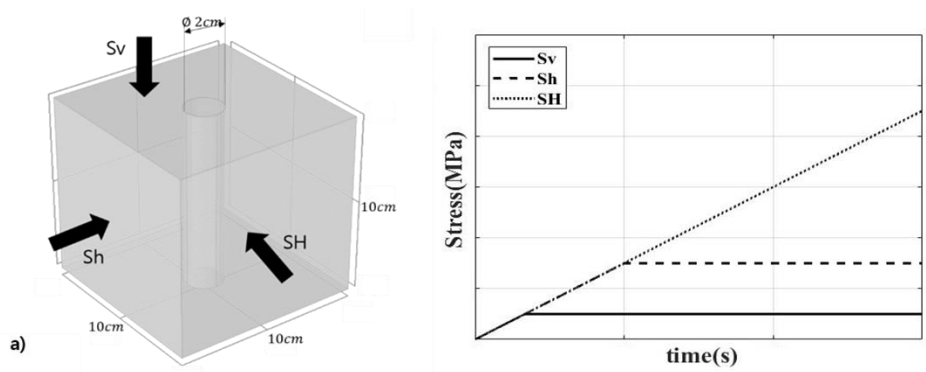

Figure 3.8: Stress direction and loading mode for true-triaxial loading test.

For heater test under confinement, loading condition was also same with loading test except that maximum horizontal stress was also maintained after targeted stress reached. After all three axis of stress has reached the targeted value, temperature of the outer walls of specimen where aligned to S_h and S_H directions were heated from 30 ℃ (room temperature) to 130 ℃. Heating rate was kept at 2℃ /min to avoid effect of transient thermal shock. Procedure of heater test and hating phase is depicted in Figure 3.9.

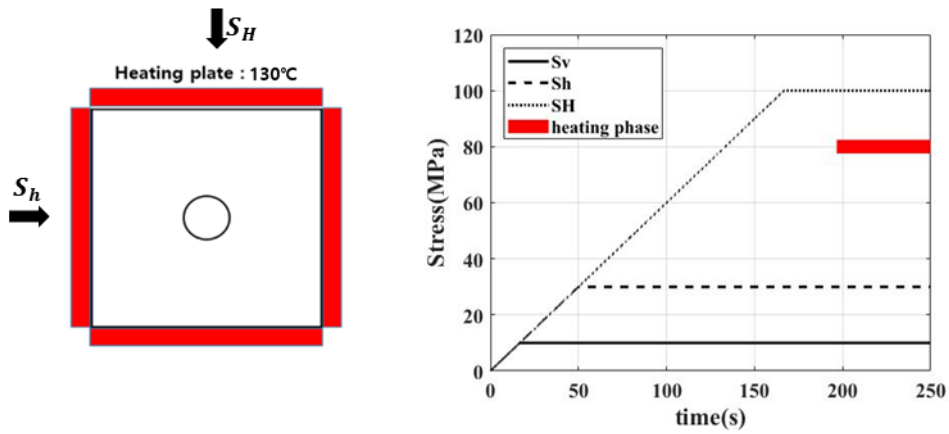

Figure 3.9: Heating direction and procedure of heater test

.

As shown in Figure 3.10, Total 12 different boundary condition tests were conducted which consists of 9 loading test and 3 heater tests. For loading tests, 9 tests are mainly categorized into two different tests which are **MH** and **MV** test. To estimate the effect of vertical stress on borehole stability, this two categorized tests were conducted by different vertical stress conditions while maintaining same minimum horizontal stress condition. Total 4 **MV** tests were conducted for minimum horizontal stress value of 10/ 14/ 18/ 22 MPa, and vertical stress was set to be equal to minimum horizontal stress. On the other hand, for MV test, vertical stress was fixed to 6MPa for all 5 different minimum horizontal stress cases which were 6/ 10/ 14/ 18/ 22 MPa.

Heater tests are named **TM** and 3 different tests were conducted as mentioned. Both tests were assigned to same vertical stress and minimum horizontal stress as 18MPa and only different maximum horizontal stress was assigned which values are 21 MPa, 30 MPa and 35 MPa respectively. The experimental scheme in this laboratory test is summarized in Table 3.2.

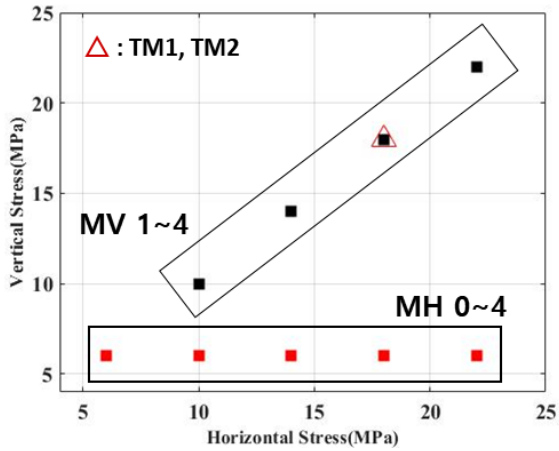

Figure 3.10: Boundary conditions for true-triaxial loading test.

Table 3.2: Experimental scheme of laboratory test.

Name	Num	S_v (MPa)	S_h (MPa)	S_H (MPa)	Temp (℃)
MH	#0	6	6	–	–
	#1		10		
	#2		14		
	#3		18		
	#4		22		
MV	#1	10	10	–	–
	#2	14	14		
	#3	18	18		
	#4	22	22		
TM	#1	18	18	21	130
	#2			30	
	#3			35	

3.2 Laboratory test result and discussion.

3.2.1 True-triaxial loading test

A typical example (MV #4) of true-triaxial loading test in this study is shown in Figure 3.11 and Figure 3.12. For all tests, It was able to define two different maximum horizontal stress level, which are S_{H1}: incipient failure and S_{H2}: one set of heavy borehole breakout. This two levels of stress state was determined by combination of visual observation where visible crack initiates and heavy spalling take place respectively, and AE data where sudden increase of absolute energy occurs.

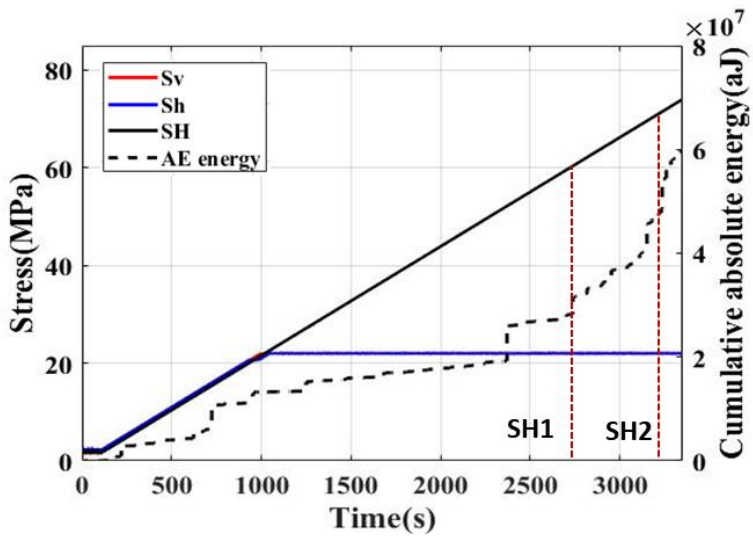

Figure 3.11: Boundary conditions for true-triaxial loading test. Stress regime and cumulative absolute energy is depicted as colored solid lines and dotted line, respectively.

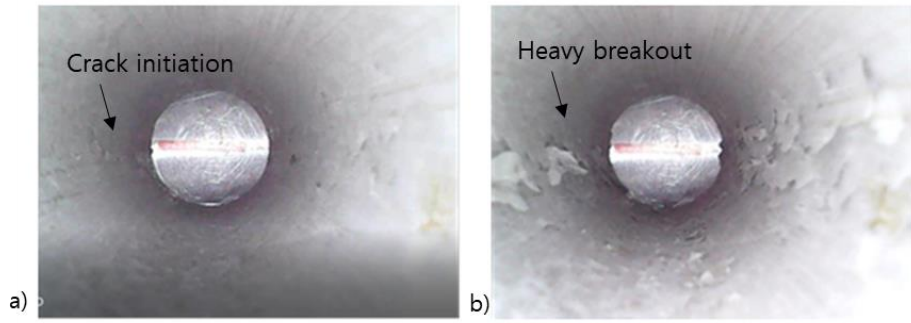

Figure 3.12 Visual observation from camera inserted inside borehole for MH#3 test during loading test. a) SH1: 60Mpa, b) SH2: 71MPa

All of the loading test results are summarized in Figure 3.13. As can be observed, both S_{H1} and S_{H2} was proportional to S_h which is consistent to relevant laboratory studies (Lee and Haimson 1993). However, important thing to notice is that the amount of this proportional increase was dependent to vertical stress. Comparing with MH tests, MV tests showed much increase in S_{H1} and S_{H2} by increase of S_h. Also, the gap between S_{H2} and S_{H1} was much larger for test MV. In addition to magnitude of maximum horizontal stress value, horizontal stress ratio (S_H/S_h) is also one of the critical parameter for borehole breakout and this value is illustrated in Figure 3.14. As the magnitude of S_h increased, starting from 6:1 of this horizontal stress ratio (S_{H1}/S_h), it decreased to 3:1 and 2:1 for MV and MH test, respectively.

This results suggest the effect of vertical stress acting along the borehole direction. In other words, when vertical stress is higher, borehole breakout initiated in much severe environment (large S_H

magnitude, large horizontal stress ratio (S_H/S_h) and borehole is more stable after incipient failure occurred around borehole wall.

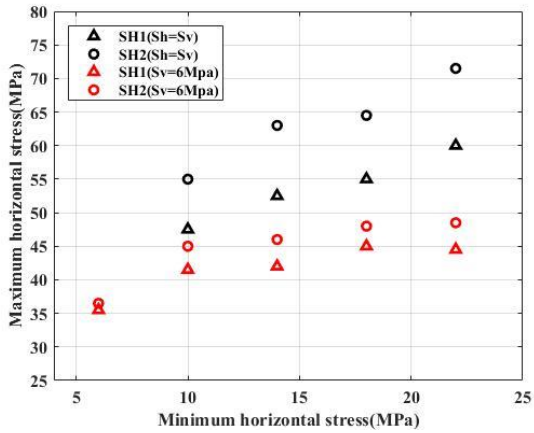

Figure 3.13 Relationship between the maximum horizontal stress and the minimum horizontal stress (S_h) required for breakout initiation (S_{H1}) and severe breakout (S_{H2}).

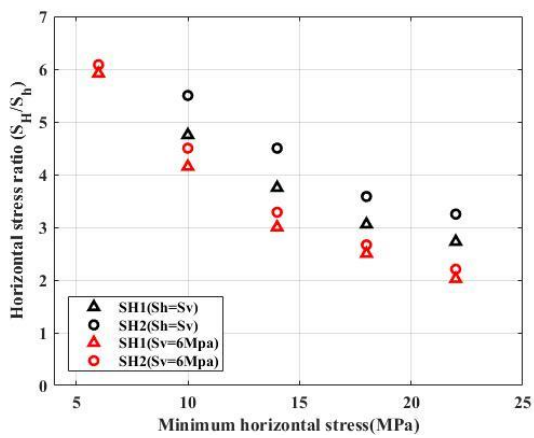

Figure 3.14: Relationship between the horizontal stress ratio and the minimum horizontal stress (S_h) required for breakout initiation (S_{H1}) and severe breakout (S_{H2})

X−ray CT scanning technique was also applied for failed specimen to quantify and qualify the borehole breakout. Typical example of CT scanning after breakout for MV#3 (S_v:S_h:S_H = 18MPa: 18MPa: 64.5MPa) and MH#3 (S_v:S_h:S_H = 6MPa: 18MPa: 64.5MPa) is compared in Figure 3.15. It was possible to observe V−shaped borehole breakout failure in laboratory test which is similar to field observation (figure 1.1). To compare tangential stress magnitude, finite element code COMSOL was applied is illustrated Figure 3.16.

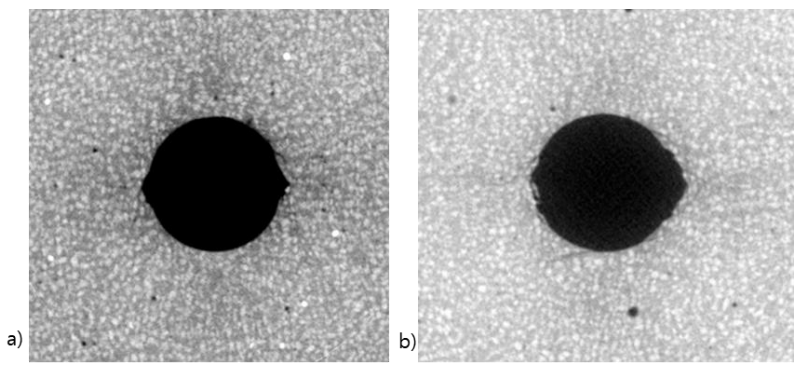

Figure 3.15: Cross section view of borehole wall from X-ray CT scanning after breakout. A) MV#3 b) MH#3

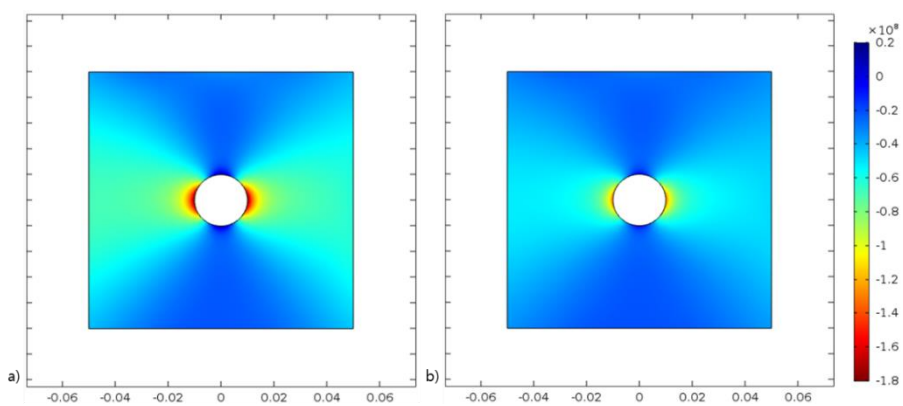

Figure 3.16: Boundary conditions for true-triaxial loading test.

Although tangential stress magnitude around borehole was much higher for MV#3 test then MH#3 test, the amount of borehole failure was more significant in test MH#3. This result also verifies the strengthening effect of vertical stress on borehole breakout.

The loading test results were compared with two different failure criteria which are Mohr−coulomb and Mogi−coulomb criterion. However, it was impossible to directly apply these criteria to the results because of scale effect. Martin (Martin 1997) summarized the previous laboratory test results and showed that there exists significant scale effect for test when borehole diameter was less than 75mm in diameter as shown in the Figure 3.17. As the borehole size increases failure was occurred when tangential stress approaches the UCS of the material. In this study, tangential stress required to initiate borehole failure was about 3 times of UCS. This is reasonable value considering range of 1.5~3 times for 20 mm borehole test was observed from previous tests. As a result, to compare with failure criteria, The UCS of mortar specimen was assumed to be 3 times of acquired value which is 120 MPa.

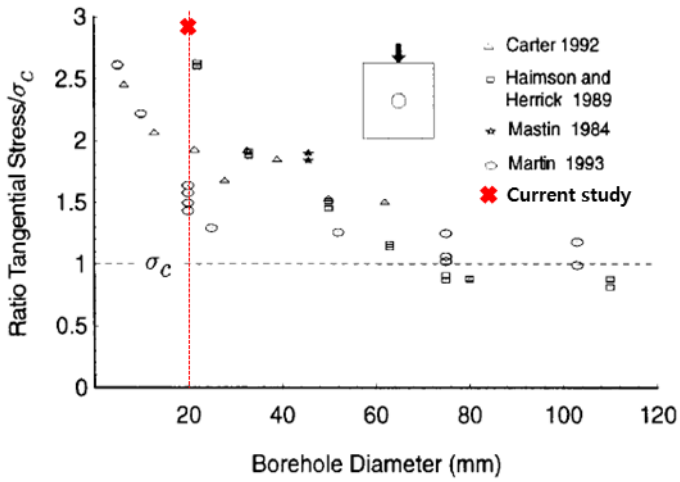

Figure 3.17: Summary of previous test results for tangential stress required for borehole breakout compared to UCS (Martin 1997).

To analyze borehole stability, one should compare stress state at borehole wall against failure criteria. The stress state at a vertical borehole wall can be given by Kirsch solution as:

$$\begin{aligned} \sigma_{rr} &= 0 \\ \sigma_{\theta\theta} &= S_H + S_h - 2(S_H - S_h)cos2\theta \\ \sigma_{zz} &= S_v - 2v(S_H - S_h)cos2\theta \end{aligned} \tag{3.2}$$

where σ_{rr} is the radial stress, $\sigma_{\theta\theta}$ is the tangential stress, σ_{zz} is the axis stress, and v is the Poisson ratio of the material. Θ is measured clockwise from the S_H direction. Therefore position for borehole breakout initiation occurs where Θ is 90 degree.

So, for a given minimum horizontal stress which ranges from 6 MPa to 22 MPa, and unknown maximum horizontal stress, principal

stresses at the borehole wall was obtained. In this case, tangential stress, radial stress, and vertical stress can be assume as maximum, minimum and intermediate principal stress, respectively. After that, by substituting obtained principal stresses to equation (2.1) and (2.2), maximum horizontal stress that requires for breakout initiation could be obtained. This values were compared with breakout initiation stress (S_{H1}) from laboratory test result as shown in Figure 3.18.

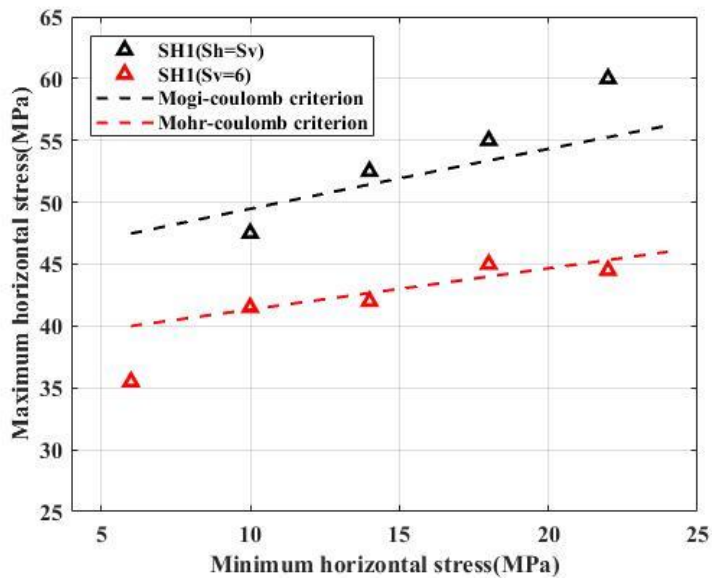

Figure 3.18: Comparison of predicted maximum horizontal stress required for borehole breakout initiation and laboratory test result (S_{H1}).

When the vertical stress was low, predicted maximum horizontal stress from Mohr-coulomb criterion matched well with laboratory test result, however, it was impossible to consider strengthening effect of vertical stress and underestimated the maximum horizontal stress for breakout initiation when the vertical stress magnitude gets higher. This means Mohr-coulomb criteria is significantly conservative in deep underground borehole where vertical stress magnitude is significant. On the other hand, Mogi-coulomb criteria could reflect the effect of vertical stress and correlated well with breakout test with increasing vertical stress. True-triaxial criteria seems to be more proper for the situation where vertical stress (or intermediate principal stress) is consequential.

However, the effect of breakout geometry on test result should be excluded to solely analyze effect of stress. According to Zang and Stephansson (2009), breakout processes in the borehole wall can be distinguished by stress magnitudes (σ_{rr} radial stress, $\sigma_{\theta\theta}$ tangential stress and σ_{zz} vertical stress) along the borehole wall as figure 3.19. Therefore stress magnitudes along borehole wall were calculated by finite element method and the result for MV#3 and MH#3 tests are depicted in figure 3.20. Although the stress magnitudes order alternates as gets far from borehole, it shows relationship of $\sigma_{\theta\theta}>\sigma_{zz}>\sigma_{rr}$ in the range where breakout occurs. This was same for all other tests which means breakout geometry is wide breakout for all tests and there is no effect of breakout geometry in this study.

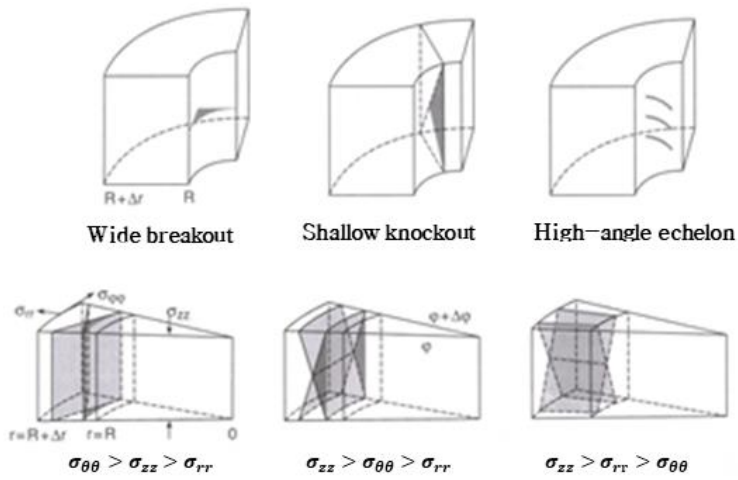

Figure 3.19: Breakout process in the borehole wall depending on the relationship between the radial (σ_{rr}), tangential ($\sigma_{\theta\theta}$) and vertical (σ_{zz}) stress magnitudes (Zang and Stephansson 2009).

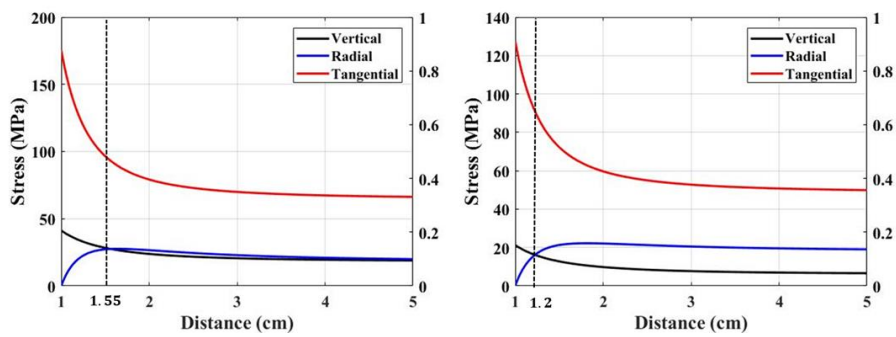

Figure 3.20: Relationship of stress magnitudes where maximum horizontal stress is $S_{H2.}$ Left: MV#3, and right: MH#3. Dotted line indicates position of breakout depth.

3.2.2 True-triaxial heater test

Typical True-triaxial heater test for TM#1 in this study is shown in Figure 3.21. For All 3 tests, additional increase of AE absolute energy was observed after temperature rise. Sudden increase of AE absolute energy occurred when outer temperature reached 130 ℃. Because of the high temperature, after raising the temperature, it was impossible to utilize camera inside borehole. So only borehole state before temperature rise was able to observe and no failure of inner wall was ensured before heating process begin.

Overall specimen state and closer observation of borehole for TM#1 and TM #2 are shown in Figure 3.22 and Figure 3.23 respectively. Unlike previous heater tests (Ishida 2004; Jansen et al. 1993b), temperature raise from outer wall condition and confining stresses prevented the tensile stress to happen from the outer surface of specimen. So, different patterns of thermal failure was identified. All tests showed extra failure at both outer surface of specimen and at inner borehole wall which named thermal breakout in this study. When TM#1 and TM#2 thermal breakout patterns were compared, since maximum horizontal stress was higher for TM#2, more severe breakout by thermal effect was occurred in TM#2 specimen. From heater test results, it was obvious that temperature recovery process could affect borehole stability issues.

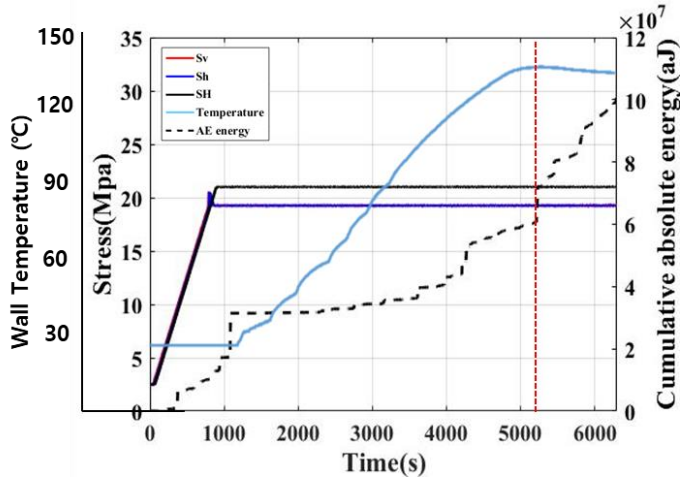

Figure 3.21: Heater test result for specimen TM#1. Sharp increase of cumulative AE energy is observed after wall temperature reached 130 ℃

Figure 3.22: Overall and close up view of specimen TM#1 after heater test.

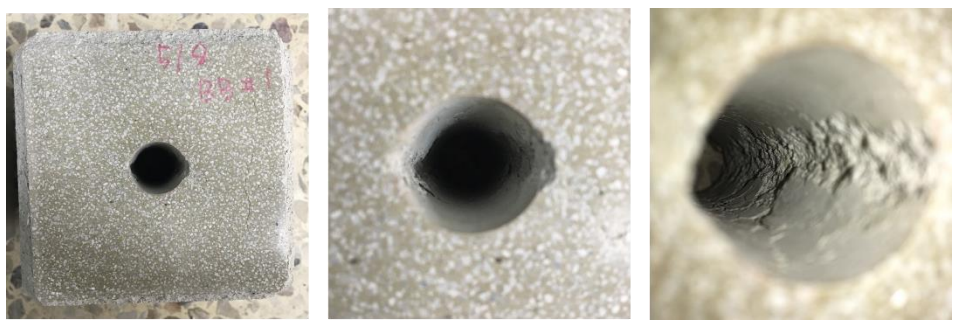

Figure 3.23: Overall and close up view of specimen TM#2 after heating test.

Chapter 4. **Numerical test**

4.1 Test description

4.1.1 Model calibration

To numerically simulate laboratory test result, attempt was made to create synthetic specimens representing cement mortar used in this laboratory study. After producing a square synthetic material, Uniaxial compression test, poliaxial compression test, and direct tension test were conducted to decide proper input microparameters of flat joint contact model to match macroproperties of cement mortar (table 3.1). Model resolution defined in this study is defined as follow:

$$\emptyset_s = \frac{W}{D_m}$$
$$\emptyset_H = \frac{D_H}{D_m} \qquad (4.1)$$

Where $\emptyset_H$ is model resolution for breakout test named hole resolution, while $\emptyset_S$ is for calibration procedure named specimen resolution. For other parameters, W is width of square specimen, D_H is borehole diameter, and D_m is the average grain diameter of the synthetic material.

According to (Potyondy 2018), macroproperties of Elastic modulus, Poisson's ratio, UCS, and tensile strength were relatively independent to grain size of flat joint contact model, so for calibration process, considering computational time, the model resolution was kept not very high which was 35 in this study. The microparameters is listed in Table 4.1. Those in the first blocks are related to material genesis (density and diameter multiplier, respectively); those in the second block are related to flat-joint contacts (installation gap, bonded fraction, gapped fraction, initial surface-gap distribution, number of elements in radial direction, radius multiplier code and value, effective modulus, stiffness ratio, friction coefficient, tensile strength distribution, cohesion distribution and friction angle, respectively); last block are related to linear group for grain-grain contact (effective modulus, stiffness ratio and friction coefficient respectively).

Table 4.1: Microparameters of cement mortar flat joint contact model.

Common group : $\rho_v[Kg/m^3]$, R_{max}/R_{min}	1850, 1.66
Flat jointed group : $g_i[mm]$, ϕ_B, ϕ_G, $(g_0)_{\{m,sd\}}[mm]$, N_r, (C_λ, λ_v), E$[Gpa]$, k_n/k_s, μ $(\sigma_c)_{(m,sd)}[Mpa]$, $(c)_{(m,sd)}[Mpa]$, ϕ[degree]	$R_{min} * 0.25$, 1.0, 0 (0, 1.0), 4, (0, 1.0}, 2.3, 1.9, 0.3 (3.7, 0.37), (2.5, 0.25), 10
Linear group : $E[Gpa]$, k_n/k_s, μ	3.3, 1.9, 0.3

* The parameters are defined in (Potyondy 2017).

Failure pattern by direct tensile test is depicted in Figure 4.1. A tensile fracture which consists of tensile cracks were formed perpendicular to the loading axis. Figure 4.2 presents the microscale damage at failure stage of UCS test, Tensile cracks subparallel to the loading axis were dominant at the first stage, which then followed by typical conjugate shear failure and finally failed.

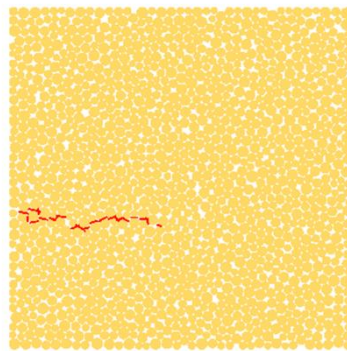

Figure 4.1: Extensile fracture at post-peak state of direct tension test with red lines representing tensile cracks.

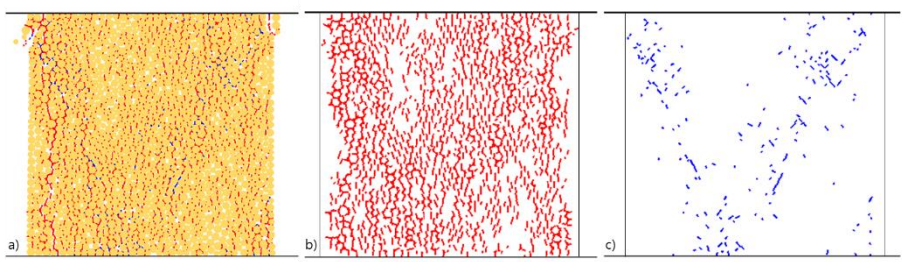

Figure 4.2: Damage at failure stage of UCS test with cracks colored red/blue for tensile/shear cracks. a) All cracks with particles, b) Tensile cracks only and c) shear cracks only.

Poliaxial test results which confining stress were 2.5 MPa/ 5.0MPa/ 7.5MPa combined with UCS test result are shown Figure 4.3. As confinement increased the material strength and ductility also increased which corresponds with typical brittle failure behavior. The macroproperties after calibration process is compared with material properties that obtained from laboratory test are listed in Table 4.2.

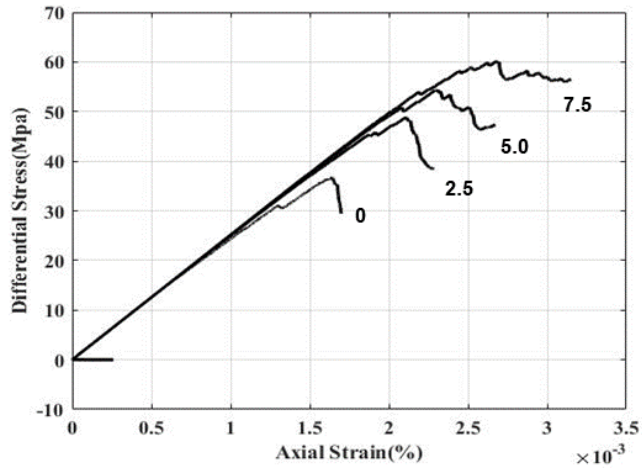

Figure 4.3: Differential stress versus axial strain during poliaxial tests. Numbers depicted are assigned confinement (MPa)

Table 4.2: Macroproperties of numerical synthetic specimen.

Properties	PFC2D	Lab test
Elastic modulus (E)	25 GPa	25 GPa
Poisson's ratio (**ν**)	0.26	0.25
Uniaxial compression strength	37 MPa	30 MPa
Brazilian tensile strength	2.2 MPa	2.3 MPa
Internal friction angle	32 °	30 °
Cohesion	10.5 MPa	10.5 MPa

4.1.2 Verification of the DEM model for thermal calculation

Thermal properties for Thermo-mechanical modeling were referred from experimentally acquired value of cement mortar specimen from (Nan 2017) and properties used in this study is listed in Table 4.3.

Table 4.3: Thermal properties of synthetic material of cement mortar. (Zhang 2017)

Properties	Value
Thermal conductivity	1.0 (W/m·℃)
Specific heat	1200 (J/Kg·℃)
Thermal expansion	$0.7e^{-5}$ (1/℃)

Alike mechanical calibration process in previous session, thermal microproperties were also required to be determined to obtain desired thermal properties. This thermal calibration process was done by comparing numerical simulation result with analytical solution. Figure 4.4 illustrates the procedure to match thermal conductivity of synthetic material (Itasca 2014). The temperature of lower boundary and upper boundary were fixed to 100 ℃ and 0 ℃, respectively. Then the temperature distribution after 600s, 3000s and at equilibrium state were compared. Analytical solution for temperature distribution at position y and time t within the sheet

is expressed as (Crank 1975):

$$\frac{\mathrm{T(y,t)}}{T_1} = 1 - \frac{y}{L} - \frac{2}{\pi}\sum_{n=1}^{\infty} e^{-\kappa n^2 \pi^2 t/L^2}\left(\frac{\sin(n\pi y/L)}{n}\right) \qquad (4.2)$$

$$\kappa = \frac{k}{\rho_t C_v}$$

where T_1 is the temperature at lower boundary, L is height of planer sheet, κ is thermal diffusivity, k is thermal conductivity, ρ_t is material density, and C_v is specific heat at constant volume. As shown in Figure 4.5, numerical simulation matched well with analytical solution for thermal conductivity 1.0 (W/m·℃).

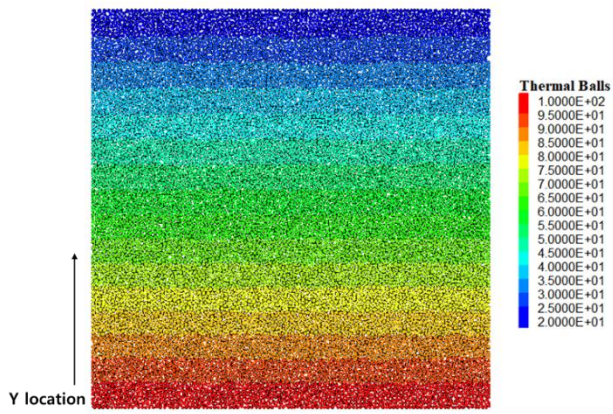

Figure 4.4: Numerical test to calibrate thermal conductivity

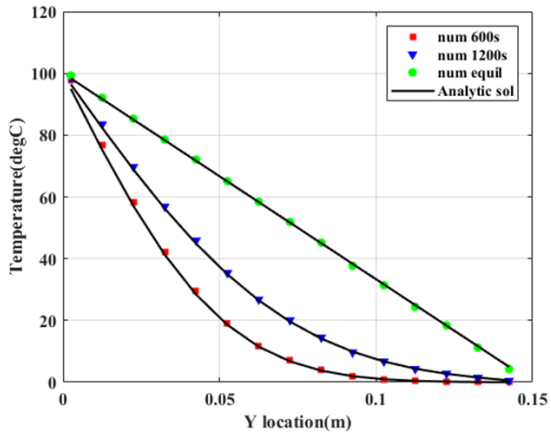

Figure 4.5: Numerical simulation and analytic solution of temperature distribution for planer sheet

Heater test within 100 mm cylindrical specimen with 10mm diameter hole was conducted as illustrated in Figure 4.6 to verify thermal stress which are related to thermal expansion coefficient. Fixed temperature boundary condition was assigned. Inner wall temperature and outer surface temperature fixed to 100 ℃ and 20 ℃, respectively. Analytical solution for tangential stress, $\sigma_{\theta\theta}$ along radial direction in cylindrical heater test is expressed by (Ishida 2004):

$$\sigma_{\theta\theta} = \frac{\alpha E}{r^2}\left[\frac{r^2 + a^2}{b^2 - a^2}\int_a^b Tx\,dx + \int_a^r Tx\,dx - Tr^2\right] \qquad (4.3)$$

where r is distance from center, E is elastic modulus, α is thermal expansion coefficient, a is hole radius and b is cylinder radius. As shown in Figure 4.7, numerical simulation matched well with analytical solution.

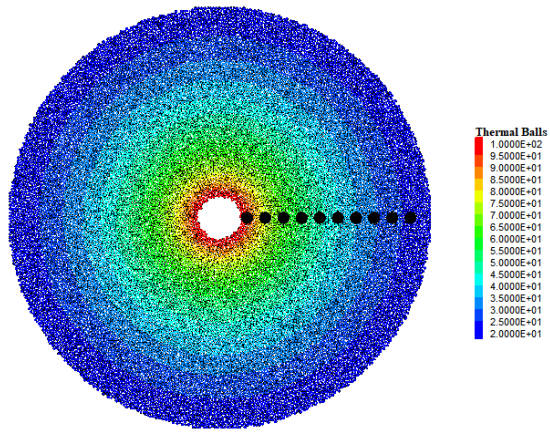

Figure 4.6: Numerical heater test verifying thermal stress. Back dots represent stress monitoring point.

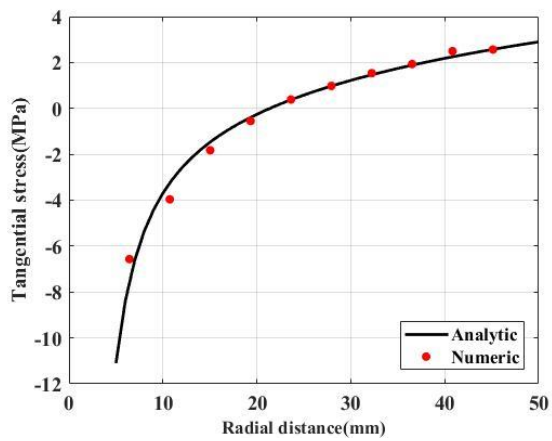

Figure 4.7: Numerical simulation and analytic solution of tangential stress for heater test within cylindrical specimen.

4.1.3 Simulation process

Overall simulation procedure is illustrated in Figure 4.8. The numerical simulation was conducted stepwise to reproduce, as far

as possible, the process of laboratory test in this study. Once the square synthetic specimen is constructed, the particles, in the rage of borehole, have deleted. No cracks were allowed during this step. Then, confining stress was applied. Same as laboratory test, minimum horizontal stress, S_h (x−axis) and maximum horizontal stress, S_H (y−axis) was raised simultaneously until S_h reached target magnitude. Then, S_H was increased monotonically while maintaining S_h till V−shaped breakout occurred. During the heating step, thermal loading took place by increasing temperature of outer surface particles. For this thermo−mechanical modeling, alike laboratory test, both S_h and S_H was conserved to set value.

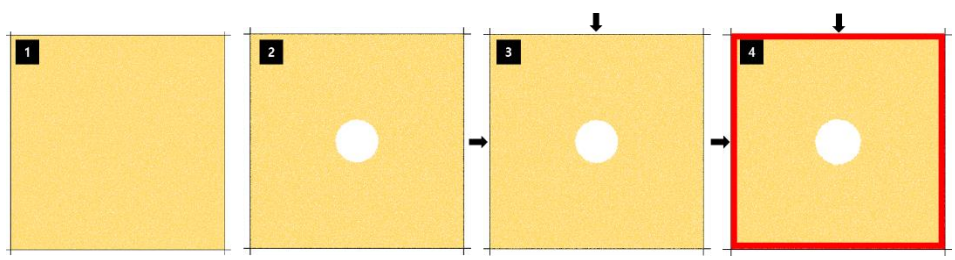

Figure 4.8: Simulation step for mechanical and thermo-mechanical modeling

The size of the synthetic material was equal to laboratory test which square width and borehole diameter are 100 mm and 20 mm, respectively. Also, breakout modeling resolution, $\emptyset_H$ was 42 for both mechanical and thermo−mechanical modeling.

4.2 Numerical test result and discussion

4.2.1 Mechanical modeling of borehole breakout

Mechanical modeling was conducted to reproduce MV#3 in laboratory experiment. Therefore, S_h was conserved to magnitude of 18 MPa. However, this modeling was done by 2D so vertical stress was not considered. Figure 4.9 to Figure 4.11 illustrates overall specimen and near borehole state when S_H is 29 MPa, 39 MPa, 43MPa, respectively. The force-chain fabric which consists of grain-grain forces, was included in the figures to recognize failure patterns readily. This fabric is depicted as colored line (black and green for compression and tension respectively and line thickness corresponding with force magnitude.

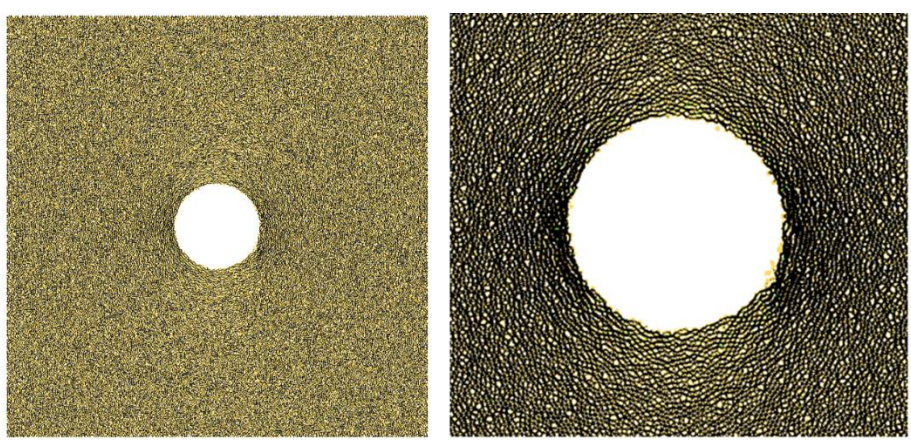

Figure 4.9: Borehole breakout simulation ($\emptyset_H = 42$). S_h = 18 MPa S_H = 29 MPa

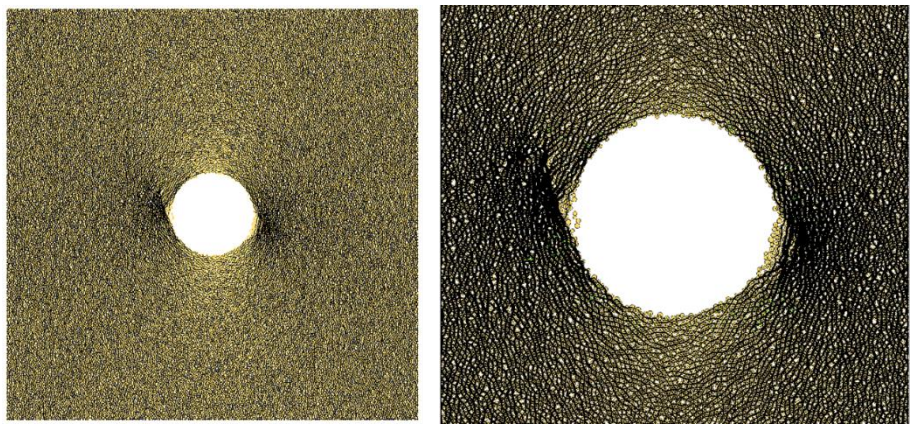

Figure 4.10: Borehole breakout simulation ($\emptyset_H = 42$). S_h = 18 MPa S_H = 39 MPa.

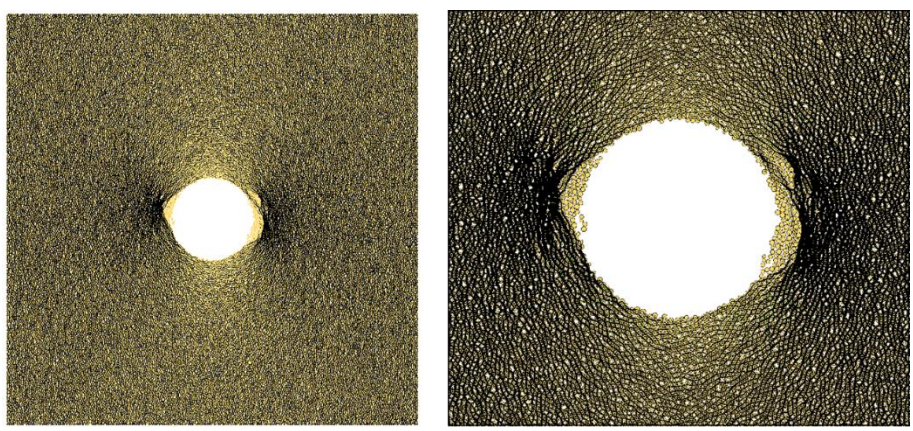

Figure 4.11: Borehole breakout simulation ($\emptyset_H = 42$). S_h = 18 MPa S_H = 43 MPa

Synthetic material showed similar behavior with laboratory test, showing symmetrical V−shaped failure, expect that the S_H magnitude to cause borehole breakout was smaller. There are two reasons that can be suggested for this discrepancy in failure stress. First is absence of vertical stress in numerical modeling. As shown in laboratory test result, vertical stress had significant strengthening

effect on borehole breakout and 2D numerical modeling was not possible to take in to account this strengthening effect. Further 3D modeling will be required to consider the effect of vertical stress. Second is scale effect. Also, observed in laboratory test, 20 mm diameter borehole test showed scale effect which made breakout to be occur at more high tangential stress. This phenomenon also can cause differences on laboratory test and numerical test.

Thin slab-like material (1-2 layer of particles) first detached and fall out into borehole at the first stage of breakout process. This could refer to spalling phenomena that was also observed in laboratory test. Then as S_H increased the opposite sides where maximum tangential stress occurs begun to soften and dilated inwardly. This process diverted the load toward the tip of the opposite notch and stabilized the breakout. This damage process was also observed by (Potyondy 2017).

In addition trend of increasing microcracks by S_H magnitude change is depicted in Figure 4.12. The tendency of microcrack growth in numerical modeling corresponded well with laboratory test result shown in Figure 4.13. Also visual observation and sudden increase of crack number were used for determining S_{H1} and S_{H2}.

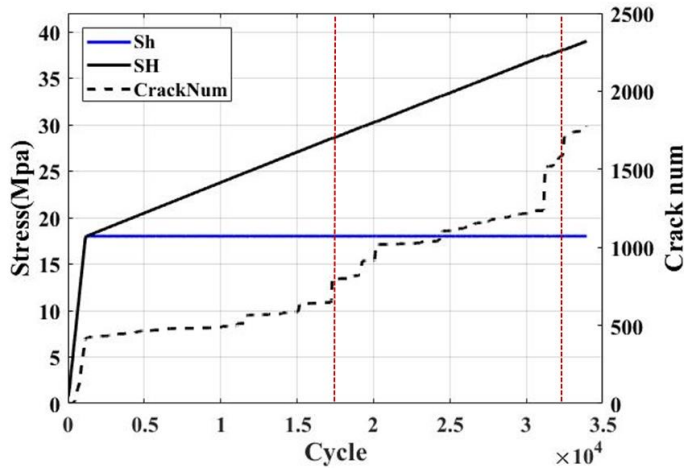

Figure 4.12: Growth of microcracks and stress regime during the numerical simulation. Case of S_h=18 MPa

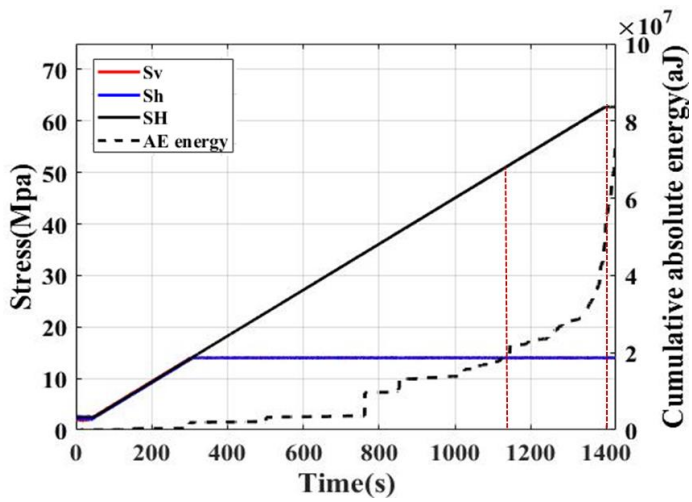

Figure 4.13: AE data and stress regime for laboratory test MV#3.

The effect of minimum horizontal stress, S_h was also studied by discrete element modeling by reproducing MV#1 laboratory stress. Therefore same simulation was conducted except setting S_h to 6 MPa. The microcrack increasing trend is depicted in Figure 4.14. As

expected, S_{H1} magnitude where breakout initiated was about 25MPa that is lower than the case of S_h=18MPa. Also, S_{H2} was also lower and the value was about 35MPa. The Growth of microcracks and breakout patterns during simulation is depicted in Figure 4.14 and Figure 4.15, respectively.

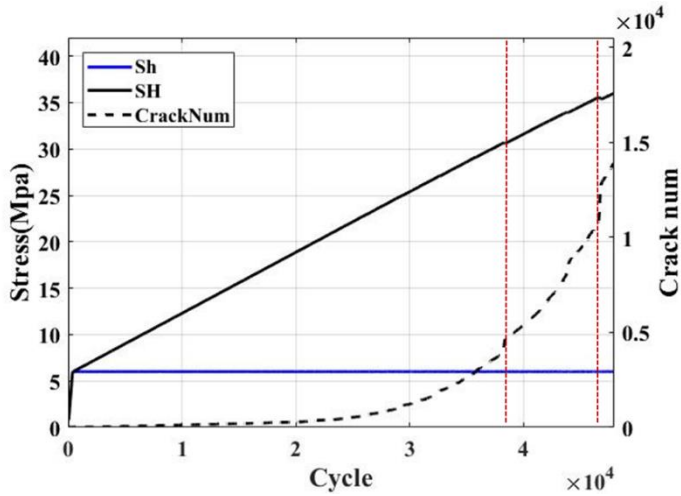

Figure 4.14: Growth of microcracks and stress regime during the numerical simulation. Case of S_h=6 MPa

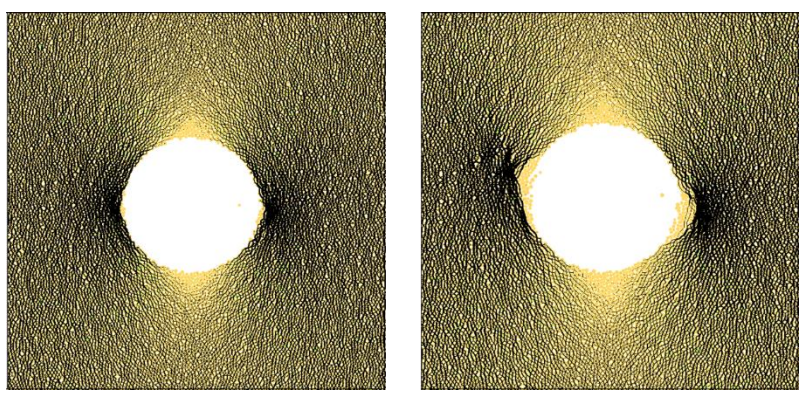

Figure 4.15: Borehole breakout simulation ($\emptyset_H = 42$). left: S_h = 6 MPa S_H = 30, right: S_h = 6 MPa S_H = 35 MPa

According to (Potyondy 2017), breakout test also affected by resolution and this was explained by concept of effective boundary. Therefore, the numerical breakout test was conducted within larger resolution, $\emptyset_H$ which is 66. The mechanical modeling result within increased resolution specimen is depicted in Figure 4.16 and Figure 4.17. The breakout pattern was irrelevant to particle resolution when the value is higher than specific value, in this case which is 44. However, for high resolution model, breakout started to occur at lower magnitude of S_H, compared to lower resolution model and this also corresponds to result by (Potyondy 2017).

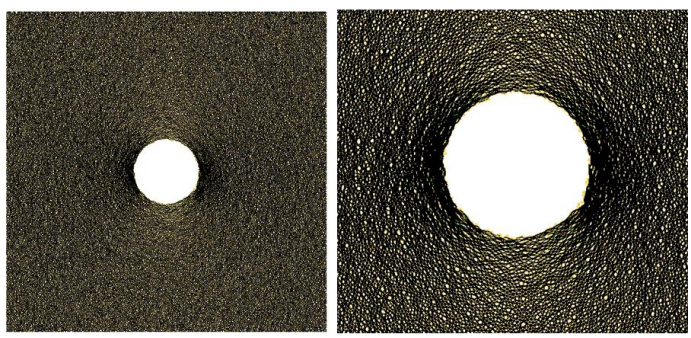

Figure 4.16: Borehole breakout simulation ($\emptyset_H = 66$). S_h = 18 MPa S_H = 26 MPa

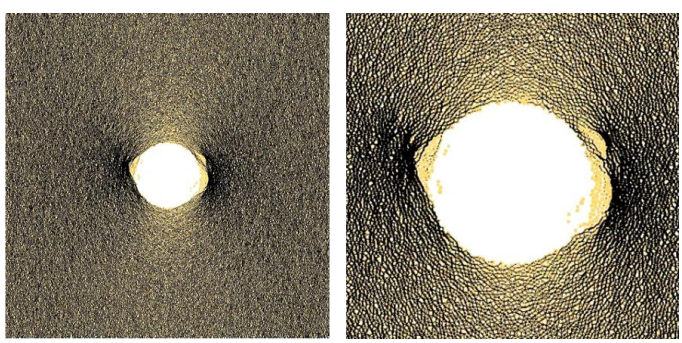

Figure 4.17: Borehole breakout simulation ($\emptyset_H = 66$). S_h = 18 MPa S_H = 40 MPa

Comparison of breakout pattern is made and illustrated in Figure 4.18. The slightly rotated failure pattern might be caused by heterogeneity of contact strength in flat joint model. However, overall pattern of breakout in numerical simulation corresponded well with laboratory test result.

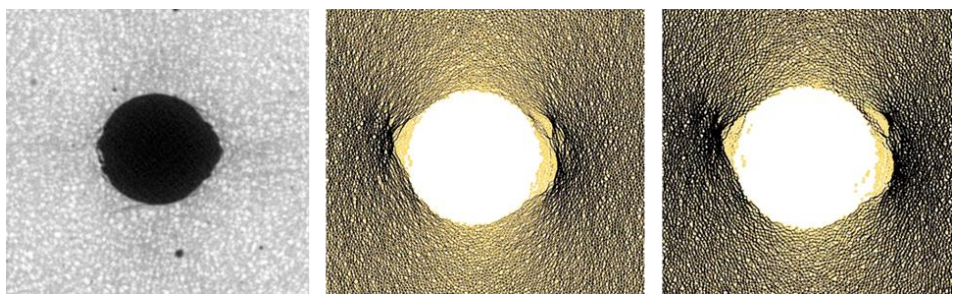

Figure 4.18: Comparison of borehole breakout pattern. CT scanning result for MH#3, 42 resolution numerical simulation at S_H = 43 MPa, and 66 resolution numerical simulation at S_H = 40 MPa, respectively

4.2.2 Thermo-mechanical modeling of borehole breakout

Following the procedure depicted in Figure 4.8, Thermo-mechanical modeling was conducted. Confining stress was set as 18 MPa and 26 MPa for S_h and S_H, respectively, since this value was the marginal magnitude of stress before borehole breakout occur. After borehole stabilized at the assigned confining stress, temperature was raised to 250 ℃ from the outer surface of synthetic specimen at 5 ℃/min rate. The initial temperature of entire specimen was 20 ℃ while borehole wall was adiabatic condition. In this thesis, results which thermal expansion value of $1.5e^{-5}$ are analyzed. This is because the failure around the borehole was too minute when thermal expansion value was $0.7e^{-5}$, which followed the Table 4.3.

Configuration of microcrack increase depending on temperature change is illustrated in Figure 4.19. Gradually increasing cracks by temperature rise was observed, but there was no sudden increase of microcrack. Also, as extra failure occurred after maximum temperature reached at outer surface in lab test, there was no extra failure for numerical simulation. In numerical test, temperature was almost fully developed to equilibrium state but not in laboratory test. So, temperature rise near borehole continued after outer surface temperature reached its targeted value in laboratory test. Difference in boundary condition at borehole and thermal conductivity can be considered for this discrepancy in simulation and laboratory test.

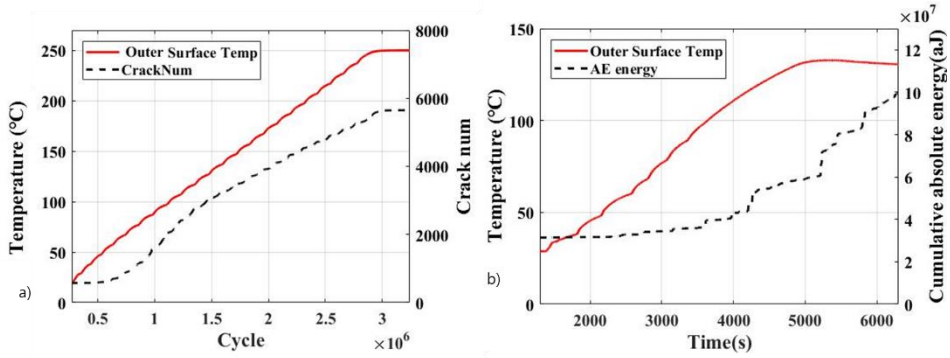

Figure 4.19: Comparison of heater test result. a) Numerical simulation, b) laboratory test TM#1.

The state of specimen during simulation is depicted in Figure 4.20. The result showed thermal cracks only developed in outer surface and around borehole, not in entire area. Tensile crack was dominated and started from outer surface of specimen and then followed by cracks around borehole which corresponded to laboratory heater test. However, although high value of thermal expansion coefficient and wall temperature were imposed, V-shaped borehole breakout was not observed as laboratory test result. In addition, to analyze the thermal failure process, Tangential stress was monitored as illustrated in figure 4.21.

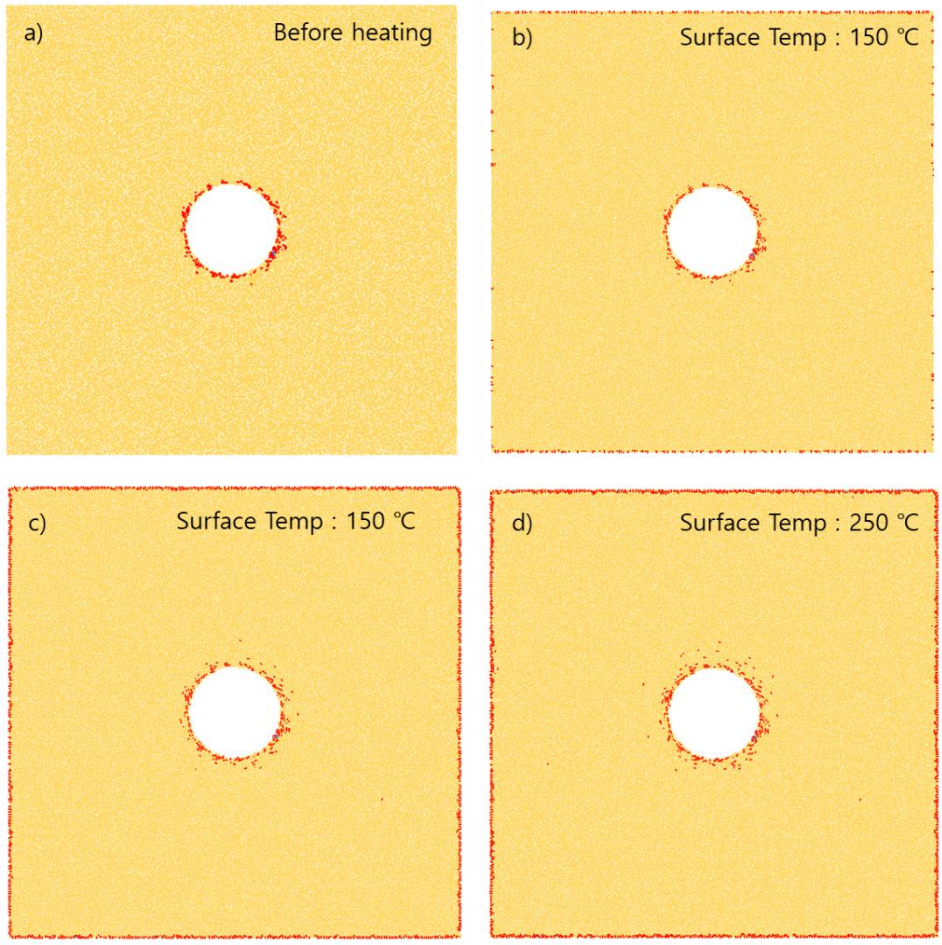

Figure 4.20: Result of thermo-mechanical simulation during heater test for a) before heating, when surface temperature reached b) 150 ℃ c) 200 ℃ d) 250 ℃, respectively. S_H and S_h magnitude are 26 MPa, 18 MPa, respectively. Each red lines corresponds to tensile cracks and blue lines corresponds to shear cracks.

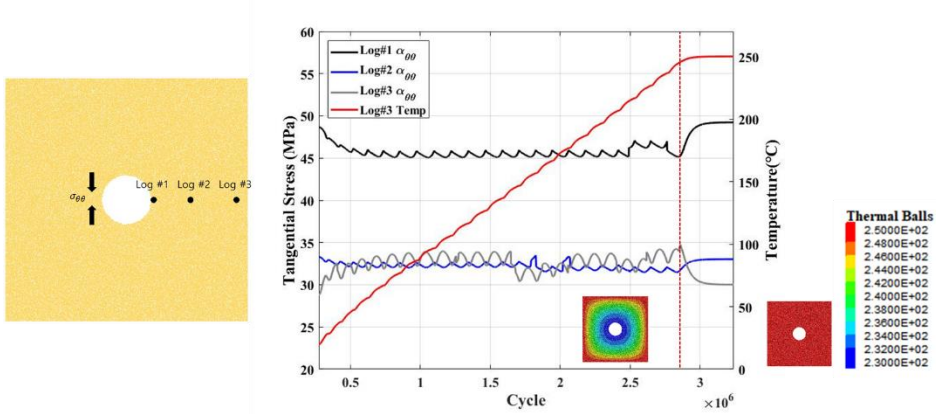

Figure 4.21: Logging location and tangential stress change according to temperature change. State of temperature distribution is also illustrated when right after surface temperature reached 250 ℃ and after reached equilibrium state.

As temperature raised from outer wall, thermal loading was produced by thermal gradient. This increased tangential stress at outer surface about 7 MPa while decreased tangential stress at borehole wall about 3 MPa. This thermal stress first caused microcracks at outer surface. Tangential stress then recovered to previous value, as temperature distribution fully developed. Since no increase in tangential stress near borehole occurred, microcrack by grain expansion can be considered as main mechanism for extra damage near borehole rather than thermal loading. Especially as only free surface is inner borehole wall, the particles tends to move inwardly by expansion, so cracks starts to occur near borehole wall. However, as mentioned previously, the failure amount was not significant as laboratory test. (Koyama et al. 2013) also found this difference of damage amount between numerical simulation and field

test. Spalling phenomena observed in the in situ experiment was not observed in 2D DEM simulation. There are several reasons that can be considered for this difference. First, In this study, thermal properties that was used can be different with real properties since the value was obtained from references and this might have affected thermo-mechanical modeling result. Second, mechanical properties of cement mortar material might change at high temperature. Lastly, the particle size and its distribution may also significantly affect the thermal crack proceeding.

For numerical simulation, additional study was conducted where temperature rise occurs in borehole wall. While previous model (Temperature rise from outer surface) reproduces the temperature recovery after drilling or injection, this model (Temperature rise from inner borehole) analogous to nuclear waste disposal system. The same boundary stress condition and procedure was adopted with Figure 4.8, except temperature was controlled by particles located perimeter of borehole wall. A specific algorithm (Shiu 2011) was utilized to detect a set of closed linked particles around the borehole. Configuration of microcrack increase depending on temperature change is illustrated in Figure 4.22. Sudden increase of microcrack number was observed when borehole wall temperature reached about 130 ℃. This was when borehole breakout occurred by temperature rise. As shown in Figure 4.23, V-shaped borehole breakout by temperature rise at borehole wall was able to observe numerically.

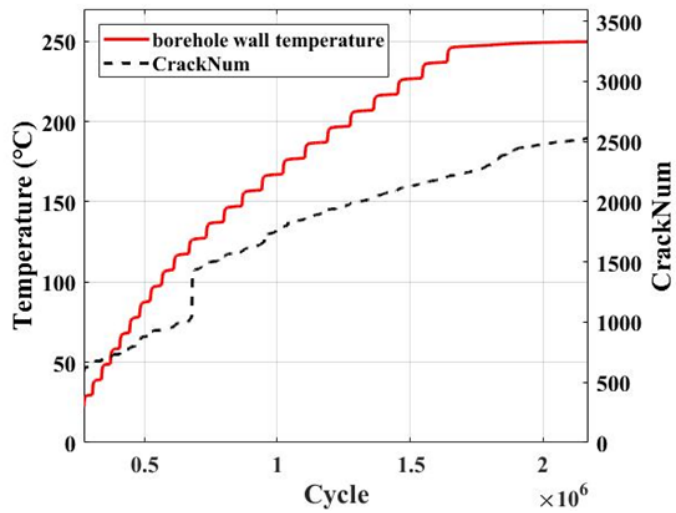

Figure 4.22: Growth of microcrack by temperature increase from borehole wall. Sharp increase of crack at wall temperature 80 ℃.

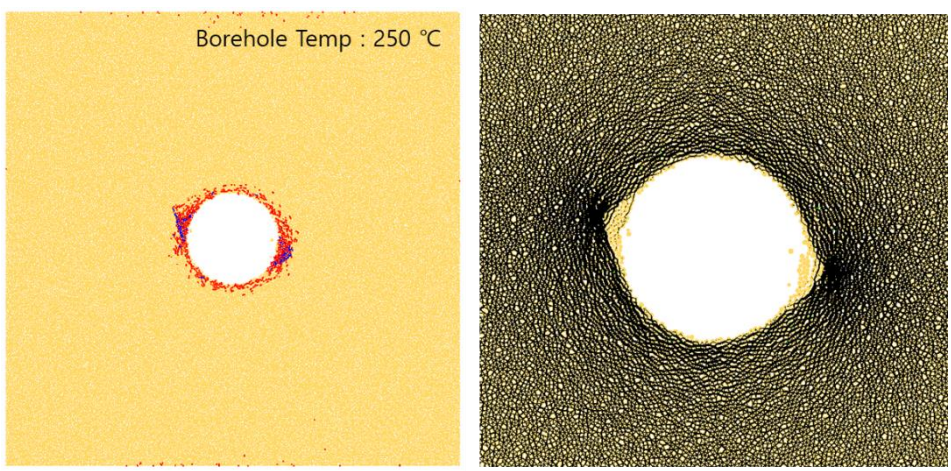

Figure 4.23: Result of thermo-mechanical simulation when borehole wall temperature reached 250 ℃. Each red lines corresponds to tensile cracks and blue lines corresponds to shear cracks. V-shaped notch was observed.

When temperature was raised from inner borehole, borehole stability was mainly influenced by thermal loading created by thermal gradient. This was different with previous case where temperature

was raised from outer surface, which main mechanism was microcrakcs by grain expansion. The tangential stress configuration during heater test is show in Figure 4.24, where logging location is same as depicted in Figure 4.21. Tangential stress increased about 10 MPa at location log#1 and dropped suddenly as breakout occurred. By contrast, Tangential stress decreased at outer surface by thermal gradient. However, this stress is expected to be recovered as temperature fully develops.

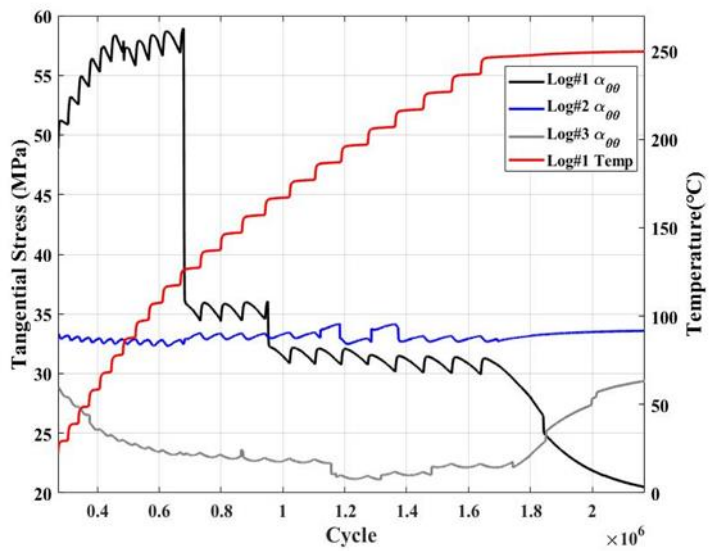

Figure 4.24: Result of thermo-mechanical simulation when borehole wall temperature reached 150 ℃. Each red lines corresponds to tensile cracks and blue lines corresponds to shear cracks. V-shaped notch was observed.

Chapter 5. **Conclusion**

Laboratory test and numerical simulation of borehole breakout under thermo-mechanical loading was carried out. Laboratory test was conducted with cement mortar specimen through true-triaxial test machine. Numerical test was conducted by particle based discrete element method and flat-joint contact model was applied.

From the laboratory test result, V-shaped borehole breakout was reproduced. It was obvious that vertical stress has strengthening effect on borehole stability issues. Large magnitude vertical stress made borehole breakout to occur at more severe stress state. In addition the failure initiation stress state at high vertical stress was well predicted by Mogi-coulomb failure criterion. Although Mohr-coulomb also well predicted the breakout initiation stress state at low magnitude of vertical stress, the discrepancy became larger when vertical stress effect increased. However, to apply failure criteria, assumption of rock strength was made by observed scale effect on laboratory test result which corresponded to previous studies. Heating test was conducted by increasing temperature at specimen surface and observed extra breakout by temperature rise.

For numerical test, the synthetic specimen was calibrated by mortar specimen used in laboratory test and verification process for determining thermal properties was carried out. Mechanical modeling

result corresponded well with laboratory result, showing similar trend of microcrack growth. V-shaped breakout was also observed from numerical simulation. The effect of particle size for analyzing borehole stability was conducted and showed that increasing resolution result in breakout at lower stress magnitude.

Two cases of thermo-mechanical modeling which are first, temperature rise from outer surface and second, temperature rise from borehole wall were carried out. For the first case, severe breakout as laboratory test result was not observed. However, extra damage by microcracks around borehole was observed numerically. By contrasts, for the second case, severe breakout occurred by temperature rise. The main mechanism that affected borehole stability was different in each case. It is microcracks by grain expansion, and increase of tangential stress by temperature gradient for first case and second case, respectively.

Reference

Al-Ajmi, A. M., and R. W. Zimmerman. 2006. 'Stability analysis of vertical boreholes using the Mogi-Coulomb failure criterion', *International Journal of Rock Mechanics and Mining Sciences*, 43: 1200-11.

Al-Ajmi, Adel. 2006. 'Wellbore stability analysis based on a new true-triaxial failure criterion', KTH.

Andersson, J. Christer, C. Derek Martin, and Håkan Stille. 2009. 'The Äspö Pillar Stability Experiment: Part II—Rock mass response to coupled excavation-induced and thermal-induced stresses', *International Journal of Rock Mechanics and Mining Sciences*, 46: 879-95.

ASTM, E. 2006. 'Standard terminology for nondestructive examinations'.

Barton, Colleen A, Mark D Zoback, and Kerry L Burns. 1988. 'In-situ stress orientation and magnitude at the Fenton Geothermal Site, New Mexico, determined from wellbore breakouts', *Geophysical Research Letters*, 15: 467-70.

Bell, JS, and DI Gough. 1979. 'Northeast-southwest compressive stress in Alberta evidence from oil wells', *Earth planetary science letters*, 45: 475-82.

Chang, Chandong, Lisa C McNeill, J Casey Moore, Weiren Lin, Marianne Conin, and Yasuhiro Yamada. 2010. 'In situ stress state in the Nankai accretionary wedge estimated from borehole wall failures', *Geochemistry, Geophysics, Geosystems*, 11.

Crank, John. 1975. *The mathematics of diffusion / by J. Crank* (Oxford, [Eng] : Clarendon Press: Oxford, [Eng]).

Duan, K., C. Y. Kwok, and M. Pierce. 2016. 'Discrete element method modeling of inherently anisotropic rocks under uniaxial compression loading', *International Journal for Numerical and*

Analytical Methods in Geomechanics, 40: 1150-83.

Ewy, Rt. 1999. 'Wellbore-stability predictions by use of a modified Lade criterion', *SPE Drill. Complet.*, 14: 85-91.

Fakhimi, A., F. Carvalho, T. Ishida, and J. F. Labuz. 2002. 'Simulation of failure around a circular opening in rock', *International Journal of Rock Mechanics and Mining Sciences*, 39: 507-15.

Gholizadeh, S., Leman, Z., & Baharudin, B. T. H. T. . 2015. 'A review of the application of acoustic emission technique in engineering.', *Structural Engineering and Mechanics*: 1075.

Haimson, B. C., & Song, . '.. A new borehole failure criterion for estimating in situ stress from breakout span. ', *Rock Mechanics and Rock Engineering.*

Haimson, B. C., and I. Song. 1993. 'Laboratory study of borehole breakouts in Cordova Cream: a case of shear failure mechanism', *International Journal of Rock Mechanics and Mining Sciences and Geomechanics Abstracts*, 30: 1047-56.

Haimson, B., and C. Chang. 2000. 'A new true triaxial cell for testing mechanical properties of rock, and its use to determine rock strength and deformability of Westerly granite', *Int. J. Rock Mech. Min. Sci.*, 37: 285-96.

Ishida, T., Kinoshita, N., & Wakabayashi, N. . 2004. 'Acoustic emission monitoring during thermal cracking of a granite block heated in a center hole.', *In Proceedings of the 3rd Asian Rock Mechanics Symposium, Kyoto, Japan, 30 November 2 December.*

Itasca, C. G. . 2014. 'Pfc2D manual, Version 5.0.', *Book Pfc2D Manual, Version, 5.*

Itasca, C. G. Itasca 2015. 'PFC3D v5. 0-user manual.', *Consulting Group, Minneapolis.*

Jaeger, J. C. 2007. *Fundamentals of rock mechanics / J.C. Jaeger, N.G.W. Cook, and R.W. Zimmerman* (Malden, MA : Blackwell Pub.:

Malden, MA).

Jansen, DP, SR Carlson, RP Young, and DA Hutchins. 1993a. 'Ultrasonic imaging and acoustic emission monitoring of thermally induced microcracks in Lac du Bonnet granite', *Journal of Geophysical Research: Solid Earth*, 98: 22231-43.

Jansen, DP, SR Carlson, RP Young, and DA %J Journal of Geophysical Research: Solid Earth Hutchins. 1993b. 'Ultrasonic imaging and acoustic emission monitoring of thermally induced microcracks in Lac du Bonnet granite', 98: 22231-43.

Keshavarz, M., Pellet, F. L., & Hosseini, K. A. . 2009. ' Comparing the effectiveness of energy and hit rate parameters of acoustic emission for prediction of rock failure.', *In ISRM International Symposium on Rock Mechanics-SINOROCK 2009. International Society for Rock Mechanics and Rock Engineering.*

Koyama, T., M. Chijimatsu, H. Shimizu, S. Nakama, T. Fujita, A. Kobayashi, and Y. Ohnishi. 2013. 'Numerical modeling for the coupled thermo-mechanical processes and spalling phenomena in äspö pillar stability experiment (APSE)', *Journal of Rock Mechanics and Geotechnical Engineering*, 5: 58-72.

Lee, H., T. Moon, and B. Haimson. 2016. 'Borehole Breakouts Induced in Arkosic Sandstones and a Discrete Element Analysis', *Rock Mechanics and Rock Engineering*, 49: 1369-88.

Lee, M., and B. Haimson. 1993. 'Laboratory study of borehole breakouts in Lac du Bonnet granite: a case of extensile failure mechanism', *International Journal of Rock Mechanics and Mining Sciences and Geomechanics Abstracts*, 30: 1039-45.

Liu, Quansheng, Jie Xu, Xuewei Liu, Jingdong Jiang, and Bin Liu. 2015. 'The role of flaws on crack growth in rock-like material assessed by AE technique', *International Journal of Fracture*, 193: 99-115.

Martin, C. D. 1997. 'Seventeenth Canadian Geotechnical Colloquium: The effect of cohesion loss and stress path on brittle

rock strength', *Canadian Geotechnical Journal*, 34: 698-725.

Michlmayr, Gernot, Denis Cohen, and Dani Or. 2012. 'Sources and characteristics of acoustic emissions from mechanically stressed geologic granular media — A review', *Earth-Science Reviews*, 112: 97-114.

Mogi, Kiyoo. 1971. 'Effect of the triaxial stress system on the failure of dolomite and limestone', *Tectonophysics*, 11: 111-27.

Nan, Zhang. 2017. 'A study on damaged zone around an opening in rock-like material due to thermo-mechanical loading'.

Park, Bona, and Ki-Bok Min. 2015. 'Bonded-particle discrete element modeling of mechanical behavior of transversely isotropic rock', *International Journal of Rock Mechanics and Mining Sciences*, 76: 243.

Park, Bona, Ki-Bok Min, Nicholas Thompson, and Per Horsrud. 2018. 'Three-dimensional bonded-particle discrete element modeling of mechanical behavior of transversely isotropic rock', *International Journal of Rock Mechanics and Mining Sciences*, 110: 120-32.

Potyondy, D. O. . 2018. 'A Flat-Jointed Bonded-Particle Model for Rock. ', *In 52nd US Rock Mechanics/Geomechanics Symposium. American Rock Mechanics Association.*

Potyondy, D. O. . 2017. 'Simulating perforation damage with a flat-jointed bonded-particle material.', *In 51st US Rock Mechanics/Geomechanics Symposium. American Rock Mechanics Association.*

Potyondy, D. O. . 2012. 'A flat-jointed bonded-particle material for hard rock.', *In 46th US Rock mechanics/geomechanics symposium. American Rock Mechanics Association.*

Potyondy, D. O., and P. A. Cundall. 2004. 'A bonded-particle model for rock', *International Journal of Rock Mechanics and Mining Sciences*, 41: 1329-64.

Read, RS 2004. '20 years of excavation response studies at AECL's Underground Research Laboratory', *International Journal of Rock Mechanics Mining Sciences*, 41: 1251-75.

Shamir, Gadi, and Mark D Zoback. 1992. 'Stress orientation profile to 3.5 km depth near the San Andreas fault at Cajon Pass, California', *Journal of Geophysical Research: Solid Earth*, 97: 5059-80.

Shiu, W., Dedecker, F., Rachez, X., & Peter-Borie, M. . 2011. 'Discrete modeling of near-well thermo-mechanical behavior during CO2 injection.', *In Proceedings of the 2nd International FLAC/DEM Symposium.*

Single, Bhawani, R. K. Goel, V. K. Mehrotra, S. K. Garg, and M. R. Allu. 1998. 'Effect of intermediate principal stress on strength of anisotropic rock mass', *Tunnelling and Underground Space Technology incorporating Trenchless Technology Research*, 13: 71-79.

Souley, M, F Homand, S Pepa, and D Hoxha. 2001. 'Damage-induced permeability changes in granite: a case example at the URL in Canada', *International Journal of Rock Mechanics Mining Sciences*, 38: 297-310.

Tingay, M, John Reinecker, and Birgit %J World Stress Map Project Müller. 2008. 'Borehole breakout and drilling-induced fracture analysis from image logs': 1-8.

Townend, J, and MD Zoback. 2004. 'Regional tectonic stress near the San Andreas fault in central and southern California', *Geophysical Research Letters*, 31.

Wanne, T. S., and R. P. Young. 2008. 'Bonded-particle modeling of thermally fractured granite', *International Journal of Rock Mechanics and Mining Sciences*, 45: 789-99.

Wanne, TS. 2009. "Bonded-particle simulation of tunnel sealing experiment." In *ROCKENG09: Proceedings of the 3rd CANUS Rock Mechanics Symposium. Toronto, Canada*.

Yuan, Shih-Che, and John Harrison. 2006. "Modeling breakout and near-well fluid flow of a borehole in an anisotropic stress field." In *Golden Rocks 2006, The 41st US Symposium on Rock Mechanics (USRMS)*. American Rock Mechanics Association.

Zang, Arno, and Ove Stephansson. 2009. *Stress field of the Earth's crust* (Springer Science & Business Media).

Zhao, Zhihong. 2016. 'Thermal Influence on Mechanical Properties of Granite: A Microcracking Perspective', *Rock Mechanics and Rock Engineering*, 49: 747-62.

Zoback, Mark D, Daniel Moos, Larry Mastin, and Roger N Anderson. 1985. 'Well bore breakouts and in situ stress', *Journal of Geophysical Research: Solid Earth*, 90: 5523-30.

초 록

심부 지하공간을 활용하기 위해서는 시추공 굴착이 필수적으로 수반되기 때문에 시추공 안정성을 유지하는 것은 매우 중요하다. 공벽파괴는 초기응력에 의한 시추공 주변 응력 재분배에 의해 발생하게 되며, 일반적으로 대칭적인 V 형태를 나타내게 된다. 더욱이, 공벽 주변의 온도변화가 큰 방사성폐기물 처분, 지열에너지 발전의 경우 온도변화에 의해 야기되는 추가적인 공벽 불안정성을 고려할 필요가 있다.

본 연구에서는 실내시험 및 수치해석적 방법을 활용하여 시추공 안정성에 대한 초기응력 및 온도변화의 영향을 파악하고자 하였다. 실내시험의 경우 20 mm 직경의 시추공을 굴착한 100 mm 크기의 정방형 몰탈시료(Mortar)를 이용하였으며 진삼축장비를 활용하여 실제 심부와 유사한 상태의 초기응력을 가해 공벽파괴를 모사하였다. 실험 결과를 통해 수평응력과 수직응력이 공벽안정성에 미치는 영향을 분석하였으며 특히, 수직응력의 강화효과 (strengthening effect)를 확인 할 수 있었다. 또한, 실험결과를 바탕으로 기존에 제시된 Mohr-coulomb 및 Mogi-coulomb 파괴 기준식과의 비교를 수행하였다. 추가적으로 진삼축이 가해진 상태에서 시료 외벽의 온도를 130 ℃까지 상승시키는 열실험을 수행하였으며 온도 상승으로 인한 추가적인 공벽파괴가 관측되었다.

수치해석의 경우 2차원 개별요소법 시뮬레이터(PFC2D)를 활용하여 실내시험 결과를 모사하였다. 응력 모델링 경우 실내 실험과 상당히 유사한 공벽파괴 과정을 재현하였으며 결과적으로 V 형태의 파괴를 나타내었다. 열-응력 모델링을 통해 시료 외벽에서의 온도상승으로 인

한 추가적인 공벽주변의 미세균열 증가 역시 모사하였으나 실내실험 결과와 비교해 적은 파괴의 정도를 나타내었다. 이러한 수치해석 결과는 이후에 시추공 불안정성에 취약한 온도 및 응력 상태를 파악하기 위한 민감도 분석의 가능성을 제시할 것으로 전망한다.

본 연구는 진삼축응력을 가함과 동시에 온도상승을 일으켜 실제 심부 시추공과 유사한 환경을 실험적, 수치해석적으로 모사함으로써 추후 터널 및 지하공간 활용 분야의 다양한 연구에 활용될 수 있을 것으로 기대된다.